3-1-2012

Flapping Wing Micro Air Vehicle Bench Test Setup

David H. Curtis

Mark F. Reeder
Air Force Institute of Technology

Craig E. Svanberg

Richard G. Cobb
Air Force Institute of Technology

Gregory H. Parker
Air Force Research Laboratory

Flapping Wing Micro Air Vehicle Bench Test Setup[*]

David H. Curtis[1], Mark F. Reeder[2], Craig E. Svanberg[3], Richard G. Cobb[4]

Air Force Institute of Technology, Wright-Patterson AFB, Ohio 45433-7765, USA

Gregory H. Parker[5]

Air Force Research Laboratory (AFRL/RB), Wright -Patterson AFB, Ohio 45433-7765, USA

ABSTRACT

The purpose of this research was to develop testing methods that can be used to determine the forces, moments, and deflections involved in flapping wing aerodynamics. To pursue the research, a flapping wing mechanism and wings with spans ranging from 9.1 inches to 12.1 inches were built. A variety of mechanisms, capable of, alternatively, purely flapping, flapping with pitch, and flapping with pitch and out-of-plane motion were conceptualized and drawn using solid modeling software. Two of the simpler designs, a single degree-of-freedom flapping mechanism and the two-degree of freedom flapping mechanism were fabricated using a rapid prototype 3-D printer, and sustained operation was demonstrated. A thrust stand and a six-component force balance were used to gather force data from the flapping-only mechanism, combined with a variety of wing shapes. Four high-speed cameras were used to capture the motion of the wings. To minimize intrusiveness an array of laser dots was projected onto the wing during flapping and photogrammetry software was used to analyze the images and determine a shape profile of the wing composed of a frame and membrane during flapping. While the focus of this research was on the bench test setup development, some insight into the influence of wing design on the forces acting on the mechanism was gained.

NOMENCLATURE

T	=	Cycle period
T_h	=	Thrust
b	=	Wingspan
P_m	=	Motor Power
n	=	Flapping frequency
ρ	=	Air Density
C_T	=	Thrust Coefficient
C_P	=	Power Coefficient
FM	=	Figure of Merit
r	=	Euclidian Distance between points in the x-y plane
w	=	Radial Basis Function Weights
$\varphi(r)$	=	Radial Basis Function
Φ	=	Matrix of Radial Basis Function solutions
Δx	=	Difference between points in the x direction
Δy	=	Difference between points in the y direction

[1] Capt., USAF,

[2] Associate Professor, mreeder@afit.edu

[3] Capt., USAF, craig.svanberg@wpafb.af.mil

[4] Associate Professor, rcobb@afit.edu

[5] Senior Aerospace Engineer, gregory.parker@wpafb.af.mil

[*] Editor's note: Prof. Haibo Dong served as Editor-in-Chief for this article

1. INTRODUCTION

Technological advancements in many fields including micro-electronics, sensors, micro-electromechanical systems, and micro-manufacturing, are leading to an increased role for small aerial vehicles, generally termed Micro Air Vehicles (MAVs). The expectation that vehicles the size of a small bird, or even an insect, can be built leads to new challenges and opportunities in experimental testing. On very small scales, there are expectations that a flapping wing design, like that of natural flyers, might be more efficient or at least might have lower observability than propeller-driven aircraft.

As with all aircraft testing, scale can affect the performance of the vehicle, both due to aeroelasticity and Reynolds number effects. However, unlike traditional aircraft tests which are ideally carried out with large models in wind tunnels to minimize these effects, MAV testing requires small but precise measurement equipment for very small scales. One of the goals of the Air Vehicles Directorate of the Air Force Research Laboratory (AFRL) is to improve their ability to comprehensively test a variety of MAV designs. As part of that goal, a collaborative effort between the Air Force Institute of Technology (AFIT) and AFRL has been undertaken to improve research and develop test methodology specific to MAV testing. Herein, we document initial phases of our efforts to explore two facets of measurement technology which are important to those who develop, test, and compare original MAV designs. Indeed, variants of the techniques we explore herein might even prove useful in characterizing natural flyers.

Our series of tests includes measurements and analysis of data acquired with a six-component balance capable of measuring the forces and moments acting on the MAV. Six-component balances are very commonly used throughout wind tunnel testing because of their fidelity, reliability, and usefulness in providing important design data. There are a number of new challenges associated with traditional balance testing for MAVs, including the competing requirements of the size limitations and the inertial load due to moving wings. Limiting factors for our 6-component balance are explored on a cursory level by comparison to data collected with a load cell and a MAV mounted to a nearly-frictionless, air bearing table in a static test environment.

While force and moment measurements would be expected to yield critical insight into the performance of a MAV, the reasons why one design might outperformed another require additional scrutiny. The second class of measurements performed relate to wing shape deformation during the flapping motion. Traditional photogrammetry methods often require either natural markings or artificial, fixed targets affixed to surfaces. This limits the utility of photogrammetry when studying the deformation of very lightweight wings. The additional weight of a fixed target is negligible for heavy fixed wing aero elastic measurement, but even ink markings can significantly alter the weight and moment of inertia of the lightweight wings used in flapping for MAVs. This motivated the implementation and enhancement of a technique for measuring three components of deformation of wings without the requirement of physical targets on the wing. Rather, a combination of laser dot projection and high speed cameras were used to capture the three-dimensional shape of the wing surface during the stroke.

Although the primary goal of our work was to explore and characterize appropriate test techniques for MAVs, one of the intermediate steps required that a mechanical flapping-wing device, mimicking a flapping-wing MAV, be well-characterized. Rather than using an off-the-shelf model, a few flapping-wing models were designed and built in-house using SolidWorks. The flapping-wing model parts were built with an Objet Eden 3-D printer and a few off-the-shelf components, such as bearings. A model which included pitch variation in addition to flapping was among the designs built. Kinematics software was used to characterize the motion of the wing for flapping mechanisms. In addition to providing a test mechanism for the two techniques described above, this procedure also enhanced our ability to design and build MAVs and their components in the future.

2. BACKGROUND
A. Flapping mechanism

There have been many attempts to mimic the flapping motion used by natural flyers. There are three primary degrees of freedom associated with flapping. In-plane motion is the up and down motion, and is perpendicular to the direction of flight. Out-of-plane motion is the motion forward and backward, and pitching motion is twisting of the wing along its primary axis. Banala and Agrawal [1] created a mechanism that is capable of all three degrees of motion. It utilized a five bar mechanism for both the in-plane and out-of-plane motion, and a four bar mechanism for the pitching motion. This allows the

mechanism to produce the figure eight wing tip pattern that insects are known to exhibit in flight. Other researchers, such as Issac, Colozza, and Rowles [2], have achieved pitching motion through the use of servomotors located in-line with the wing, while others have used torsional springs in-line with the wing to study the affect of passive pitching caused by the inertial and aerodynamic loads[3].

B. Force measurement

Wilson and Werely [3] used load cells that utilized strain gauges in their experiments to measure flapping wing lift. They directly applied the load cell to the root of the wing in such a way as to measure the lifting force. Force data were taken over the entire cycle and averaged to give the overall lift at a given frequency. Singh and Chopra [4] utilized a similar technique to measure the aerodynamic and inertial loads with strain gauges. They set up the strain gauges along the root of the wing so that the two orthogonal bending moments could be sensed. With this method they were able to determine the forces that were acting on the wing in the directions normal and tangential to the wing chord throughout the stroke. In order to translate this data into a more useful coordinate frame, in terms of lift and thrust, they used a Hall effect sensor to determine the location of the wing within its cycle corresponding to the force data. Another method involved mounting the flapping mechanism such that frictionless motion was allowed in the vertical and horizontal directions. Linear position sensors were then used to determine the axial and lift forces[5].

C. Photogrammetry

The process of using multiple synchronized cameras to capture three dimensional data about wings in flapping motion is not a new one. Stewart and Albertani [6] have done work in which a Visual Image Correlation (VIC) system has been used to determine the deformation of flexible flapping wings. A random speckle pattern was applied to flexible wings, as well as to a rigid plate that was fixed to the inboard section of the wing. The rigid plate gave a reference to the rigid motion of the wing due to the flapping. Using the speckle pattern on the rigid plate, the software is able to determine 3D data which can be used to create a transformation matrix. This transformation matrix is applied to the 3D data acquired from the speckle pattern on the flexible wing to determine the deformation data for the wing. Other techniques have been proven that use uniform printed, or sticker targets to determine deformation data. One problem with these techniques is that the added mass of the targets can be significant for the lightweight wings required on flapping wing MAVs. A solution may be projecting an array of dots onto the wing with a laser, and then using traditional photogrammetry and videogrammetry techniques to analyze the 3D locations of the points. This method has been successfully demonstrated on Gossamer space structures by Pappa, Black, Blandino, Jones, Danehy and Dorrington [7]. Because they were investigating motion of large membranes, they were able to utilize a white light projector that projected an array of targets. To our knowledge this method has not been attempted for high frequency flapping wings.

Variation in the span during flight occurs in nature, with, for instance, Pennycuick [8] showing through video analysis that the span during the upstroke of a cormorant was approximately 70 percent of that for its downstroke. Hong and Altman [9] have shown that wings with spanwise camber demonstrate an ability to produce greater lift than similar straight wings. Analysis of flow velocity data captured through PIV demonstrates that during the downstroke the cambered wing produces more positive lift force than the straight wing, while during the upstroke the cambered wing produces less negative lift force than the straight wing. This phenomenon was further investigated through the use of the laser dot projection technique.

Lasers have been used in other ways to measure the flow around flapping wings as well as their shape. Heathcote, Martin, and Gursul [10] used a laser sheet and particle image velocimetry (PIV) to investigate the flow field around wings of varying flexibility flapping in water. The laser sheet illuminated the particles in the fluid as well as the wing. The phase lag between the leading edge and the trailing edge was measured, force data were taken, and the benefits of flexibility to thrust production were shown. Rojratsirikul, Wang, and Gursul [11] used a laser sheet and high speed cameras to study the deflection and mode shapes of membrane airfoils at different angles of attack. Lui, Kuykendoll, Rhew, and Jones [12] used a laser scanner on a FARO arm to give 3D surface representation of the wings of various birds. The surface profiles then allowed them to give a detailed description of the wing motion by looking at high speed video of the birds in flight.

3. EXPERIMENTAL PROCEDURE

Before experimentation could begin, a flapping mechanism needed to be designed and built. Three different mechanisms, each capable of an additional degree of motion, were designed. SolidWorks was used as a design tool. This tool allowed the mechanism parts to be designed, and the pieces to be assembled before they were physically produced. When the design was completed, an Objet Eden 500V three-dimensional printing machine was used to fabricate the mechanism parts. Once the mechanisms were designed and built, testing could be completed. The test setup involved a six component force balance, four Photron MC2 High Speed Digital Cameras, and two laser diodes. This combination of instruments gives the capability of studying the forces and deformations involved in the operation of flapping wing micro air vehicles.

A. Wing design and construction

Two different wing types were used for the tests reported here. Initial testing using a load cell and air bearing table for force measurement was done using the wings shown in Figure 1. These wings were constructed using carbon fiber rods for spars and structural support, and Mylar® was used for the membrane material. The wing spar was a carbon fiber rod with a diameter of 0.05" for added stiffness, while smaller carbon fiber rod with a diameter of 0.04" was used for the root chord and diagonal spar pieces. The frame was created and laid over the Mylar® which was then attached to the carbon fiber rods using thin layers of lightweight adhesive tape. This had a negligible impact on the inertial and aeroelastic properties of the primary materials. A small brace is used to connect the corner leading edge to the root chord. The edges of the wing were reinforced with a piece of clear tape to prevent tearing. Four sets of wings were constructed at varying sizes, but all with an aspect ratio of two [14].


Figure 1. Carbon Fiber Wings with Mylar Membrane. Wing #1 — Spar length = 4" Chord Length = 2" Wing Span = 12.1". Wing #2 — Spar length = 3.5" Chord Length =1.75" Wing Span = 11.1". Wing #3 — Spar length = 3" Chord Length = 1.5" Wing Span = 10.1". Wing #4 — Spar length = 2.5" Chord Length = 1.25" Wing Span = 9.1".

A second set of wings was developed so that the effects of spanwise camber and the laser dot projection technique could be investigated. These wings have the same dimensions as wing number 3 from Figure 1, and are shown in Figure 2. Natural rubber latex provided a membrane material that was opaque, so that the laser dots could be easily seen when projected on it. The latex material used was approximately 0.006 inches thick, had a tensile strength of approximately 400 psi, and an ultimate elongation of 750%. A rectangular frame was selected which provides support around the entire planform of the wing, not just along the leading edge and the root chord as in the first wing set. It was desired to test both stiff and flexible wings as well as wings that were alternatively straight and with spanwise camber. Aluminum tubing (0.0625" OD, 0.0587" ID) was used for the tube frame wings, and six strands of (0.01" diameter) stainless steel wire twisted together were used for the wire frame wings.

The aluminum tube frame wings were relatively stiff while the wire frame wings were flexible to the point that flexure was visible throughout the stroke. Spanwise camber was applied to wing sets of each frame material such that the ratio of the straight line distance from root to tip to the distance

measured along the frame from root to tip along the curve of the wing was approximately 0.95. As a point of reference, the work of Pennycuick suggests that the span of a cormorant during flight, when normalized by the maximum span, varied from 0.7 to 1 during the stroke, demonstrating that birds apply spanwise camber in flight [8].
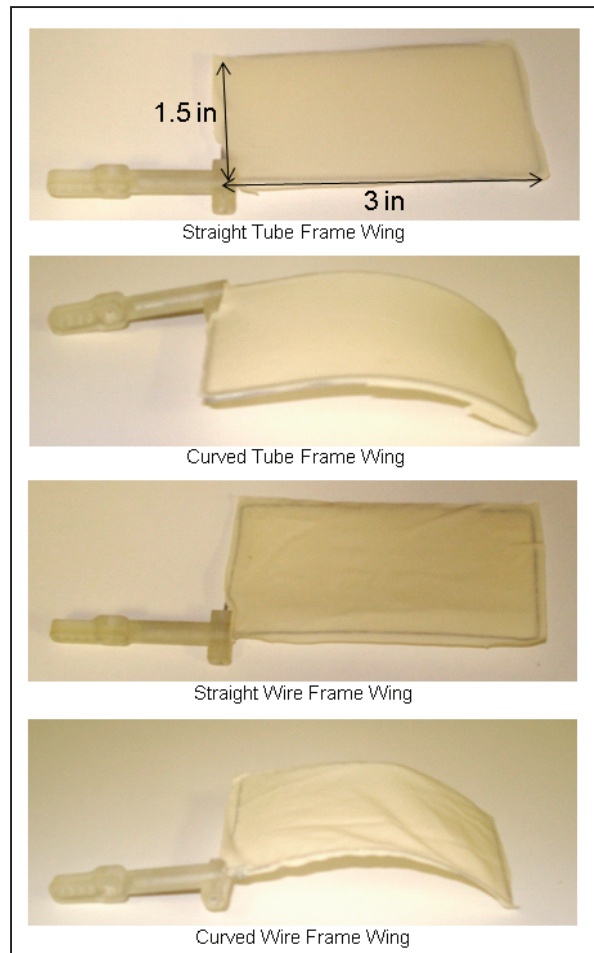
Figure 2. Wire and Tube Frame wings with Latex Membrane. Tube framing is aluminum tube with 1/16"OD. Wire frame is 6 strands of stainless steel wire (0.01" diameter) twisted together.

The pivot arm of the flapping mechanism was modified so that both an extension of the leading edge and an extension of the root chord could be secured to the pivot piece. This was done because preliminary tests of designs in which only the leading edge was secured led to drastic bending at the connection location. The Latex membrane was attached by spreading out and pinning latex to a board. The frame was sprayed with spray adhesive and then pressed onto the Latex. The glue was allowed to dry for approximately 1 hour, at which point the latex was trimmed around the frame.

Review of test results from these wing sets lead to the desire to look at a wing with a combination of stiffness and flexibility. For this reason, a wing was developed that was a hybrid of the two different frames. Aluminum tubing was used for all portions of the wing except the trailing edge and half of the tip chord, for which a single strand of stainless steel wire was used. Figure 3 shows the hybrid wing frame design. Latex was used for the membrane and was attached as before. This wing design allowed for some flexibility of the wing while keeping the overall planform of the wing relatively constant during flapping.
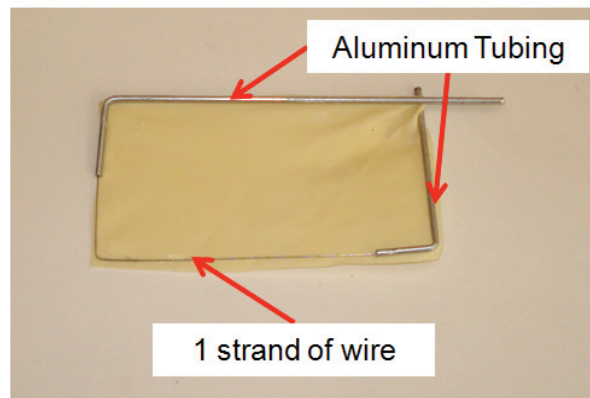
**Figure 3.** Hybrid frame Wing with Latex membrane.

B. Force measurement

Force measurement was done in two different ways. Initial testing was done using a linear air bearing table. The air bearing table provided a nearly frictionless platform on which to mount the flapping mechanism. A strain gauge transducer load cell was mounted to the rigid frame of the air bearing table such that the force from the frictionless platform could be measured. The air bearing table was angled slightly so that the load cell was preloaded. This was a simple and inexpensive way of getting good data for averaged thrust produced.

Tests were completed for the four different carbon fiber and Mylar wings described in Section III.C using this method. Twenty runs were done for each wing. For each run the load cell reading was taken at even intervals throughout the frequency range used for the wing. The frequency range of each wing was based on the mechanism capability. Larger wings require more power and therefore could not be flapped at the high frequencies that were used for the smaller wings.

The second method of force measurement was a six component force balance made by Modern Machine and Tool Co. The balance measures the following forces and moments: normal force in the range of +/- 4 lbs (+/- 1814 g), axial force in the range of +/- 2 lbs (+/- 907g), side force in the range of +/- 2 lbs (+/- 907g), pitch moment in the range of +/- 2 in-lbs (+/- 23,043 g-mm), roll moment in the range of +/- 2 in-lbs (+/- 23,043 g-mm), and yaw moment in the range of +/- 4 in-lbs (+/- 46,043 g-mm). A National Instruments data acquisition system and Labview 8.5 were used to collect the data. The six channels of the balance were connected to six of the eight available channels on a SCXI-1314 terminal block in accordance with the force balance manual. The terminal block was then connected to a SCXI-1520 universal strain gauge input module. This system is specifically designed for use with Wheatstone bridge based strain gauges. An excitation voltage of 5V was used. Initial analog signal conditioning was accomplished within the SCXI-1520 hardware for each channel individually. The signal is amplified in accordance with the anticipated voltage range specified by the user. The anticipated voltage range was given in the calibration book for the force balance provided by the manufacturer. The calibration book by the balance manufacturer provides conversion constants from output voltage to lbs (or in-lbs). An adjustable anti-aliasing low-pass analog filter is applied to the signal within the SCXI-1520. High frequency data were not required so the low-pass filter was set to 100Hz. A sampling rate of 200 Hz was used. Signal Processing was performed using a Matlab script. A 6 x 27 force interaction matrix for the balance supplied by the balance manufacturer was applied to the voltage data during post processing, however no dynamic calibration was performed.

This method was used for force measurement of the wire and tube framed latex membrane wings described in Section III.C below. Tests were completed for the four different wing types. First, wing sets were attached to the mechanism, giving an overall wingspan, b, of approximately 10" (0.254m). A tare data set was taken with the flapper motionless. Next the voltage to the flapper motor was turned up until the flapper started moving. A data set of approximately 16 seconds was taken with the force balance. The voltage was again increased, and a new data set was taken. This was repeated approximately seven times. The lowest frequency at which the mechanism can continuously operate is approximately 3 Hz. This limit is due to the need to overcome the static friction in the mechanism. The highest frequency is based on the weight of the wing, and was approximately 7.5 Hz for the wings examined in these tests. For each wing, 10-12 trails were run as described above.

In addition to processing mean values for the six components, accounting for balance interactions and the tare, spectral content was determined. The normal force and the axial force were averaged. The frequency of the given data set was determined from spectral analysis. A block size of 1024 was used, which produced 512 frequency data points over the Nyquist range of 0-100 Hz. A 50% overlap was chosen, and the PSD values from each block averaged. Each data set contained enough points for at least five averages using this method. The frequency location of the first peak of the averaged PSD was taken as the frequency of flapping for that data set. This method gives the average flapping frequency for each data set to within approximately +/- 0.1Hz. An example PSD for the normal force is shown in Figure 4.
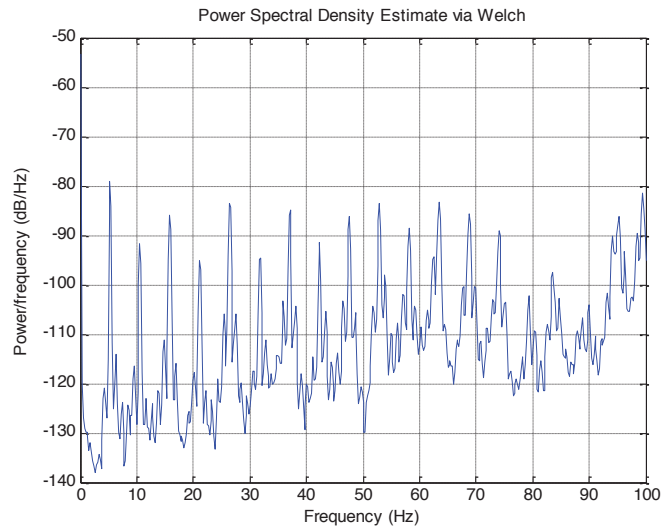
Figure 4. Power Spectral Density of Normal Force measurement from Force Balance. Data for wire frame wings at approximately 5.2 Hz flapping frequency. Sample rate = 200 Hz Block size = 1024.
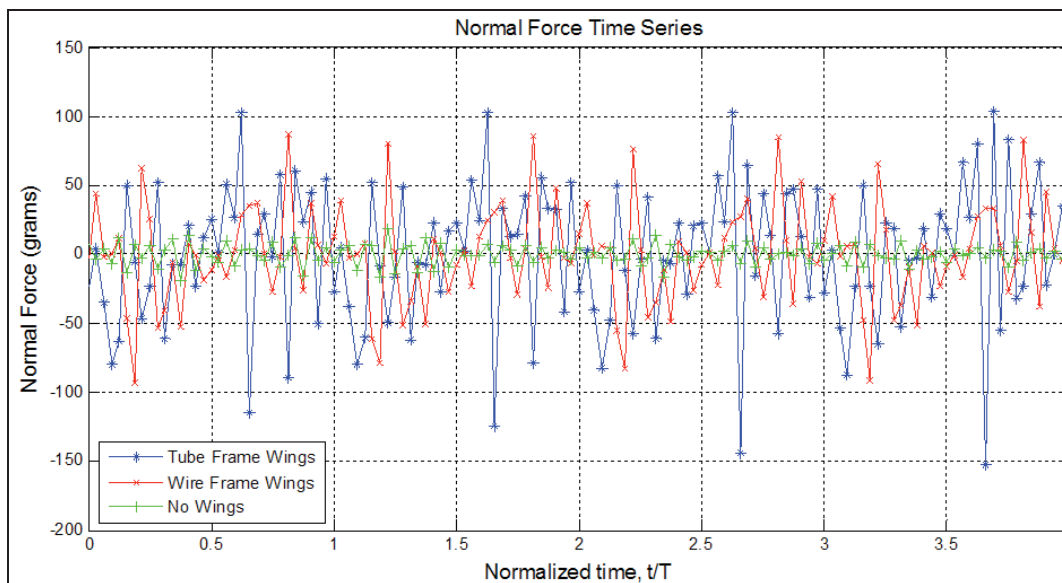
Figure 5. Temporal Normal Force Data for Normal Force. Data for four flapping cycles taken at 6.25 Hz flapping frequency for stiff tube frame wings, flexible wire frame wings, and mechanism with no wings attached.

Only time averaged axial and normal force data is presented in the results section, although time accurate data were taken for each of the 6 channels of the force balance. Time resolved normal force data is shown in Figure 5 for the straight stiff wing set and the straight flexible wing set. There is also

data taken from operating the mechanism with no wings attached, which indicates that the forces are not a remnant of the inertia of the flapping mechanism. The data were taken at 6.25 Hz, data is presented for four cycles, and time is normalized by the flapping period. This demonstrates that the balance is measuring the cyclic nature of the forces involved in flapping. More work is planned to improve the implementation of the time-resolved balance data because the data acquisition rate (200 Hz) is somewhat low compared to a typical flapping frequency. Here, the focus was placed on mean force data analysis.

C. Photogrammetry

The photogrammetry and force balance test data were acquired in AFRL's microAVIARI bench test laboratory. A high speed synchronized camera system was used for both photogrammetry and to show the operation of the mechanism and deflection of the wing. Four Photron MC2 high speed digital cameras were used to capture images of 512x512 pixels. The photogrammetry analysis software package used was PhotoModeler 6 by Eos Systems Inc. All of the cameras were focused on one wing. The software only requires two cameras to determine the three dimensional location of each point so the cameras were set up such that two camera were focused on primarily on the upper half of the stroke, and two cameras primarily focused on the lower half of the stroke. Most of the marker grid was visible in images from all four cameras for the analyzed portion of the mid-stroke. Images to be used for photogrammetry were taken at 1000 frames per second. The high frame rate requires a low exposure time, which required the aperture to be completely opened in order to get enough light.

Although no additional light was needed to see the laser dots on the wing, additional lighting was used so that other features of the images could be distinguished, such as the reference grid. Calibration of the cameras was accomplished at the end of each test period. The calibration is done to account for the focus, aperture, and zoom settings of the lens, as well as lens aberration. Images of the calibration grid provided with the PhotoModeler software were captured at multiple locations and angles for each camera.

Two laser diodes operated at 7 mW were used for dot projection. A projection head was attached to each laser which created a seven by seven square structured light dot array for each laser, giving 98 total points for the combination of two lasers. The two lasers were mounted above the wing such that the best coverage throughout the stroke was achieved. This was difficult because of the fact that the projected dot array on the wing varies with the distance of the wing from the laser. The laser array overall size increases as the surface moves away from the laser, so good coverage was achieved in the middle of the stroke, but coverage became sparse at the bottom of the stroke. For our purposes this was adequate, but because the lasers are relatively inexpensive additional lasers could have been purchased and focused on the bottom of the stroke to alleviate this problem. Improvement in this area could also have been achieved by straightening the laser array with a lens at the desired size. Once the cameras and the lasers were set-up, the flapper was turned on and images were recorded. The lasers provided targets approximately 5-10 pixels in diameter depending on the camera zoom and the angle at which the laser strikes the surface. The laser dots were relatively circular for most of the stroke analyzed, although they became elongated near the bottom of the stroke where the laser hit the surface at a high angle. The frequency of flapping was estimated from the phaser strobe but was verified by checking the number of images for a complete stroke of the wing. For analysis, a stationary frame of reference with known dimensions needs to be visible from each camera. To meet this requirement a small piece of balsa wood was marked with dots every 0.25" and attached to the top of the mechanism motor.

Photomodeler 6 was used to analyze the images taken with the high speed cameras. First the calibration images were used to create four calibrated cameras. A PhotoModeler Video (PMV) project was then set up in which the images to be analyzed were imported and matched to the calibrated camera used to capture the images. The laser dots and the reference frame dots were designated using sub-pixel marking. This is a precise method for marking the center of the light or dark multi-pixel targets. Many of the dots were referenced automatically by the software, but some were missed and needed to be done manually. Once all of the dots on all the images were sub-pixel marked, they were referenced together. Referencing is done by telling the program which points in different images correspond to the same point in space. When enough images are manually referenced, PhotoModeler was able to orient the photos, meaning that 3D position information is assigned to each point. The reference dots were then used to identify the origin, the scale, and the x and y axis direction. The 3D points are then adjusted to the assigned coordinate system [13].

Each point is assigned a residual when the epoch, or group of photos representing a given time, is processed. A table of residual values is a valuable tool to determine if there are points with large marking residuals. Marking residuals are discrepancies between where a mark is on a given photo and where the program believes the mark should be from its location on the other photos. Errors in marking and referencing were corrected until all of the residuals were less than one pixel for each camera view. Once an epoch was processed successfully, a tracking tool was used to move to the next epoch. PhotoModeler has two options for tracking points, 2D tracking and 3D tracking. The 3D tracking option was used. In this method the initial point for search in the photos in the new epoch is found by projecting the 3D position of each point from the previous epoch onto the photos in the new epoch. For the most part, the automated tracking method accurately tracks and references the points, but it is not perfect. To keep the accuracy of referencing, and marking in each epoch, the tracking was done one frame at a time. The time consuming nature of the process limited analysis to only portions of the stroke.

One of the drawbacks of laser dot projection versus printed dot photogrammetry is that when the targets are projected onto the surface they move along the contour of the surface. Meaning that for each image in time, a given laser dot is in a different place on the surface of the wing. This allows for an overall view of changes in the wings contour, but does not allow for the deflection data of each point on the wing. When viewing the three dimensional position of the points after processing, boundaries cannot be determined using only laser dot projection. To help with this visualization, additional points were added at each corner of the wing. Since there was no target on the corners of the wing these points were not sub-pixel marked; they were manually placed on the image where the corner appeared. Inconsistency in this marking method increases the inaccuracy of the corner points, although the accuracy of the corner points is not as critical as they only serve as a reference frame to help visualize the outline of the wing.

4. MECHANISM DESIGN

A mechanism utilizing crankshafts and push rods was developed. An electric rotary motor drives two crankshafts, one for each wing. The crankshafts contain a push rod that turns the rotary motion into an up-and-down motion. Connecting the other end of the push rods to a pivot arm creates the basic flapping motion desired. Three mechanisms were designed in SolidWorks. The first mechanism designed is a one degree of freedom flapper that only produced motion in the stroke plane. Only one crankshaft and rod are required for this motion. The mechanism is capable of adjustments of the flapping angle by adjusting where the push rod connects to the pivot. All testing was done with a +/- 45 degree flapping stroke. SolidWorks allows parts to be assembled, and for motion to be imparted on the total assembly of parts. This enabled us to design parts, assemble the parts, and test the mechanism operation to ensure the pieces will work together before actually producing the pieces. Figure 6 shows the one dimensional flapping mechanism as it was designed in SolidWorks.
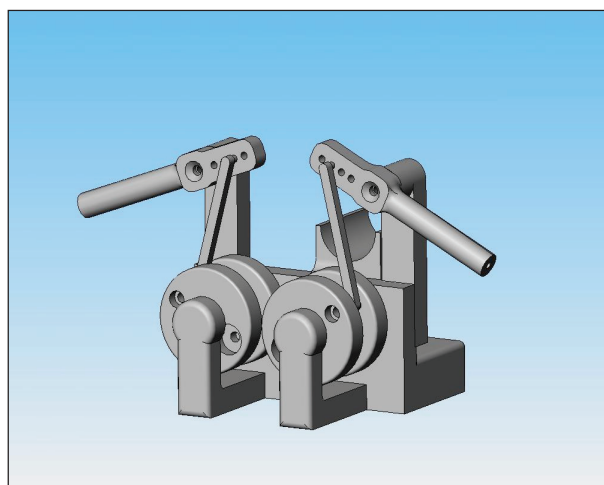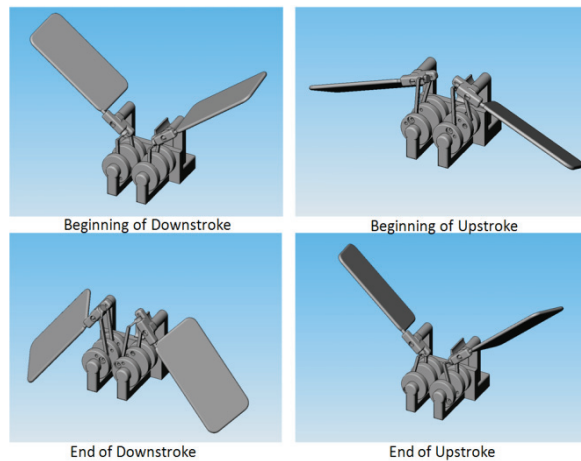

Figure 6. SolidWorks rendering of One Degree of Freedom Flapping Mechanism

   The two degree of freedom flapping mechanism is shown at four stages of its flapping cycle in Figure 7. SolidWorks was used to determine the location of the leading and trailing edge of the tip throughout the stroke. This information was used to calculate the pitch angle, which is presented throughout the stroke in Figure 8. As can be seen, the pitch angle is such that the leading edge is below the trailing edge for the majority of the downstroke, while the leading edge is above the trailing edge for the majority of the upstroke. Dickinson, Lehmann, and Sane illustrated the benefits for thrust production by adjusting the pitch of the wing during the stroke [15]. By rotating the wing to keep a positive angle of attack throughout the stroke, thrust is produced throughout the stroke.

Figure 7. SolidWorks rendering of Two Degree of Freedom Flapping Mechanism
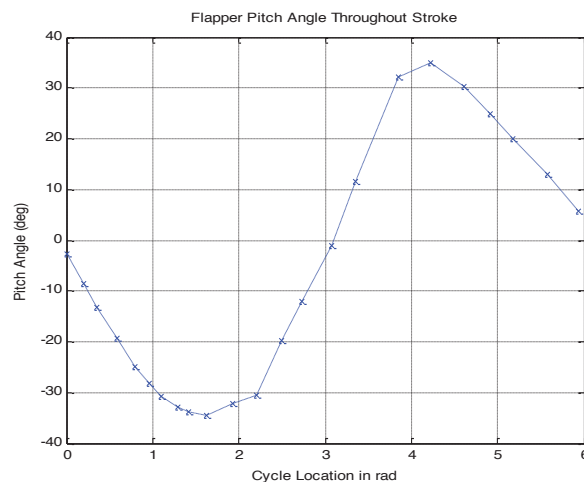
Figure 8. Pitch angle throughout stroke for two degree of freedom mechanism computed with SolidWorks

   The third mechanism designed using SolidWorks was capable of all three desired motions, flapping in-plane, pitch, and out-of-plane motion. In order to accomplish the out-of-plane motion with the same basic crankshaft design, the arm that holds the pivot point must also be allowed to rotate. A third crankshaft with a third push rod was added. The third push rod was set horizontally, and rotates the arm that holds the pivot point. As drawn, the mechanism would be capable of +/-16º flapping, +/-32º pitching, and +/-6.5º out of plane motion. The mechanism movement and tip tracking, assuming solid body motion, is shown in Figure 9 and Figure 10. All of the parts for the one degree of freedom flapping mechanism except the push rods were fabricated using an Eden Objet 500V 3-dimensional printer. An off-the-shelf swivel ball link and micro ball joint combination were used for the pushrods.

A Faulhaber DC motor with a 7 tooth pinion gear and two 48 tooth gears glued to the crankshaft were used to power the mechanism. Ball bearings were used in all of the rotating joints. Two 2-56 socket head cap screws pass through the swivel ball and connected the two halves of the crankshaft. The completed mechanism is shown in Figure 11, although the pivot arms were changed out to better secure the wings for testing. The total mechanism weights approximately 67 grams, with 23 grams of the weight attributed to the motor. The two degree of freedom mechanism was built in the same way. It uses the same push rod parts and the same motor. The flapping-pitch mechanism has a final weight of 77g and is shown in Figure 12. Naturally, these weights are too high for a flight vehicle of this size but are suitable for a bench setup.
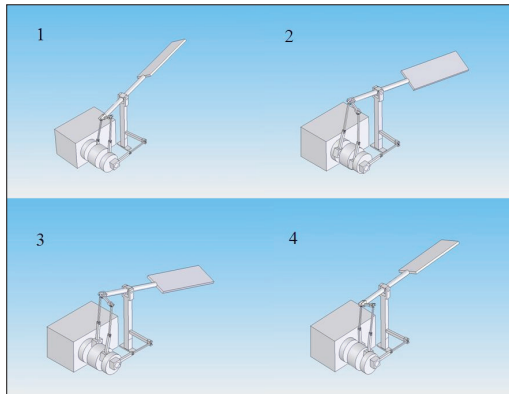
Figure 9. Three Degree of Freedom Flapping Mechanism
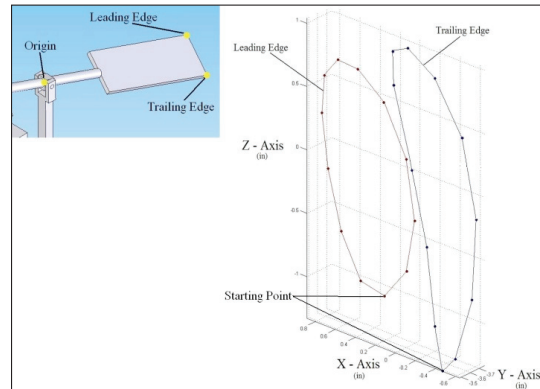
**Figure 10.** Three Degree of Freedom Wing Tip Tracking
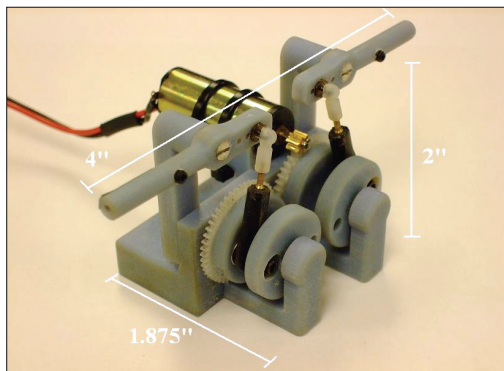
**Figure 11.** Completed one Degree of Freedom Flapping Mechanism
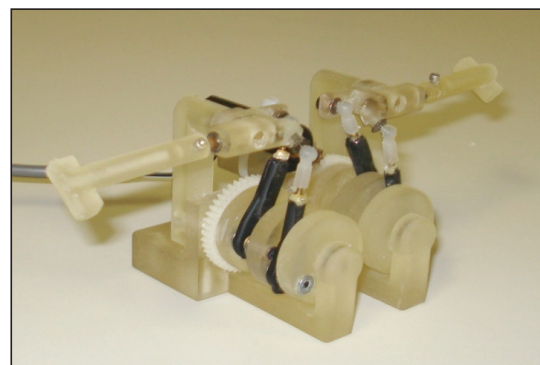
Figure 12. Completed two Degree of Freedom Flapping Mechanism

Although most of the tests reported upon in this paper were collected using the one dimensional flapping mechanism, the flapping-pitch mechanism was built and tested. Its operation was captured by high speed video from four camera angles, and single frames during one cycle of its operation is shown in Figure 13. Here, and figures to follow, the length of one cycle period, T, was verified by checking the frames where the wing was at essentially the same position. The fractional periods (e.g. T/4, T/2, and 3T/4) were determined by the frame number. Due to factors such as gear slop, wing deformation, and possibly even motor unsteadiness, the position of the leading edge of the wing at T/4 and 3T/4 do not precisely match. The straight tube frame wings were used in this demonstration. Images were captured at 250 Hz, and the mechanism was operated at 6.1 Hz. Images from camera 2 clearly show the pitching motion, which was expected based on the projected solid body motion, of the wing during the stroke.
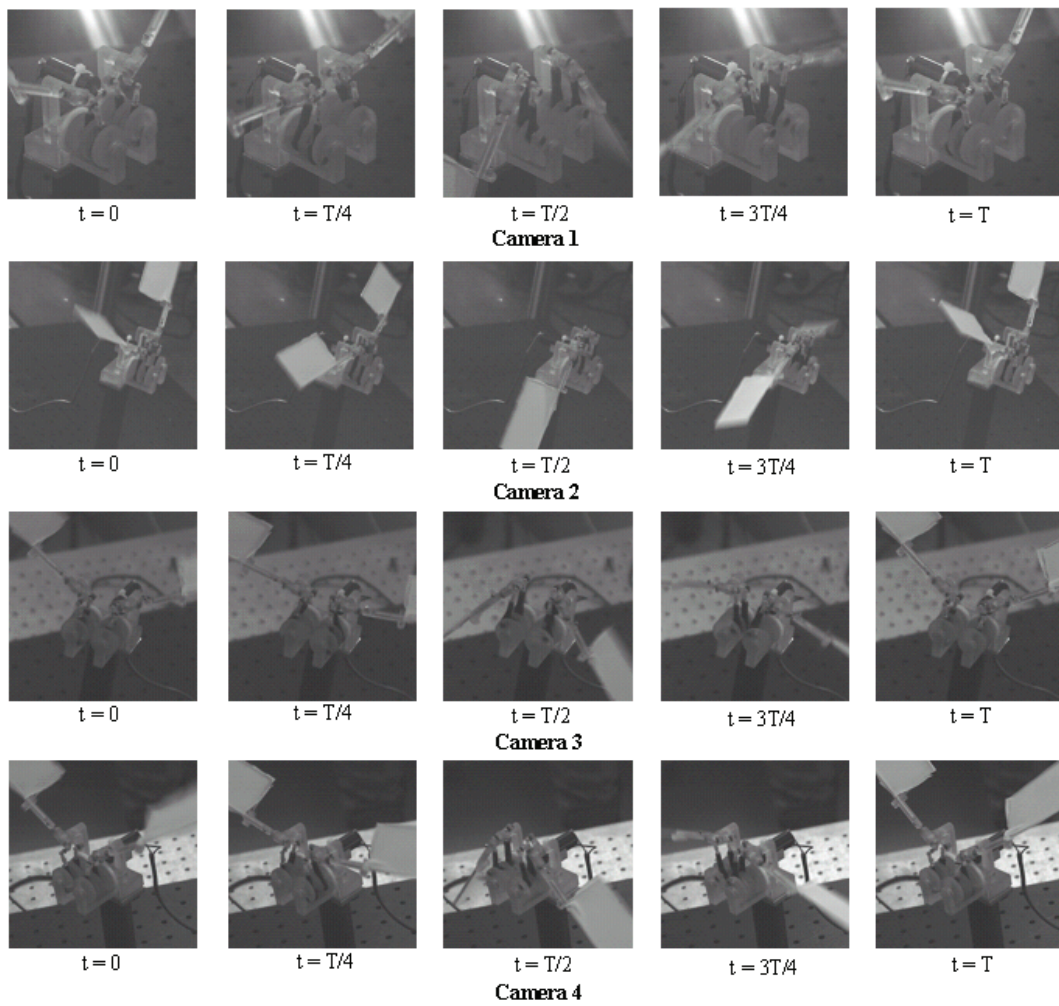
Figure 13. Two Degree of Freedom Flapping Mechanism Operation at 6.1 Hz. Images captured at 250 fps, T is the flapping period.
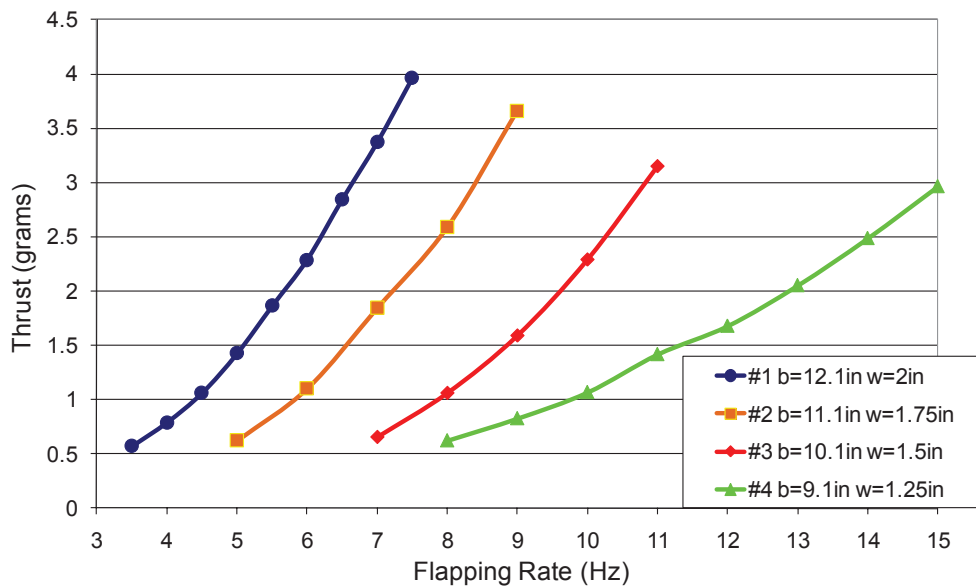

Figure 14. Thrust, in grams, plotted against flapping frequency, Hz, for 4 different sized carbon fiber frame wings.

5. RESULTS
A. Load Cell Force Measurement

The load cell, used in combination with a flapping mechanism mounted on an air bearing table, captured average thrust measurements for the carbon fiber frame wings shown in Figure 3. The four different wings are different sizes, but remain geometrically similar with the same aspect ratio. Figure 14 shows the average thrust produced for the four different wing sizes. As would be expected, thrust increased with increased flapping frequency in every case, and the highest thrust was produced with the wings with the highest surface area. The average motor power requirement to produce the thrust is shown for each wing in Figure 15. The motor power, P_m, was calculated by multiplying the voltage and current inputs to the motor for each case. Increasing thrust requires an increase in power. The slope of the lines in Figure 15, or the rate at which the power requirement increases with increased thrust is measure of the efficiency of the wing.
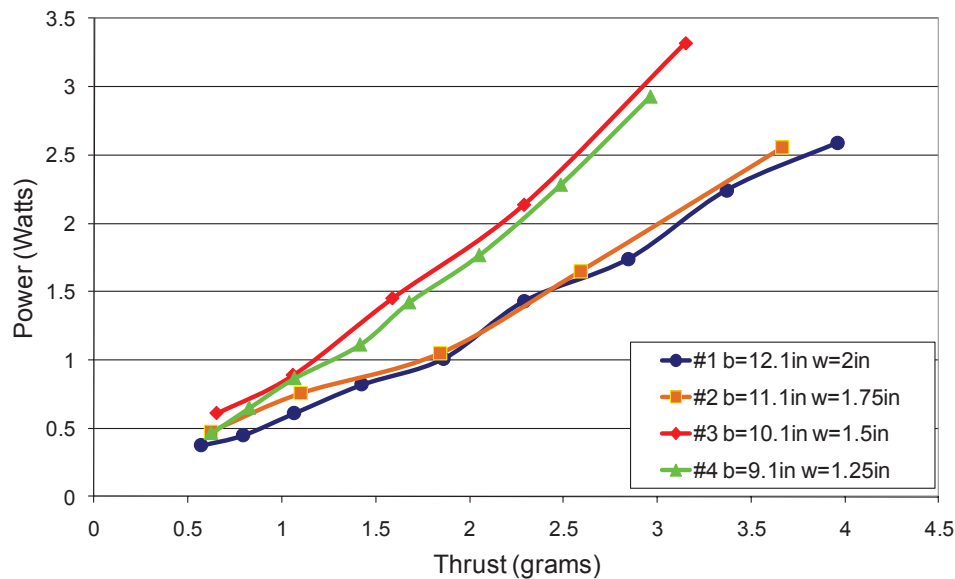
Figure 15. Motor power, Watts, plotted against thrust produced for 4 different sized carbon fiber frame wings.

Another way of measuring performance, taken from the rotorcraft applications is the figure of merit [16]. The figure of merit is calculated using the thrust coefficient, C_T, and power coefficient, C_P, as described in Equations 1-3 below.

$$C_T = \frac{T_h}{\rho n^2 b^4} \tag{1}$$

$$C_p = \frac{P_m}{\rho n^3 b^5} \tag{2}$$

$$FM = \frac{C_T^{1.5}}{\sqrt{2}C_P} \tag{3}$$

Thrust, T_h, is in Newtons, frequency, n, is in Hz, wingspan, b, is in meters, and motor power P_m, is in watts. Figure 16 shows the figure of merit plotted against thrust for each of the four wings tested. The figure of merit for each configuration tested is relatively low. The purpose of this testing was not to optimize a design that would result in the highest figure of merit, but to show that calculating this parameter is possible for flapping wing MAVs [14]. Also, the use of voltage and current to calculate power, as opposed to shaft horsepower based torque and motor shaft speed, leads to motor inefficiencies affecting the data. When plotted against raw thrust, the figure of merit collapses to a

reasonable degree for each of the geometrically similar wings, though the general trend is toward higher efficiency for the larger wings. While using a figure of merit to assess performance of the wings is important, it must be recognized that in flapping-wing flight, both thrust and lift production must be taken into account. Lift was not measured with this experimental apparatus, and thus the research effort was ultimately directed toward utilizing a six-component balance.
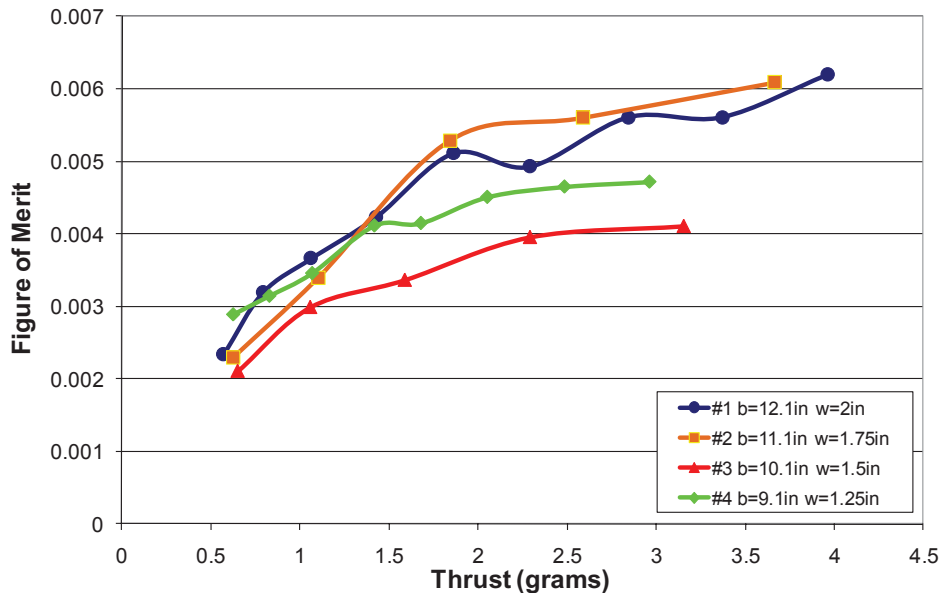

Figure 16. Figure of merit plotted against thrust for 4 different sized carbon fiber frame wings.

B. Force Balance Measurement

The force balance measurement technique provides the capability of measuring all six forces and moments simultaneously with time accuracy. Figure 17 shows axial force data, with reference to standard wind tunnel terminology, acquired using one set of wings with the load cell and data acquired with the force balance taken at the same time. The axial force is negative since thrust (in the positive x-direction) is generated with the flapping wings. The load cell validated the capability of the balance, as small differences could be attributed to friction in the air bearing table, or disruption of airflow from the wings by the balance stand.
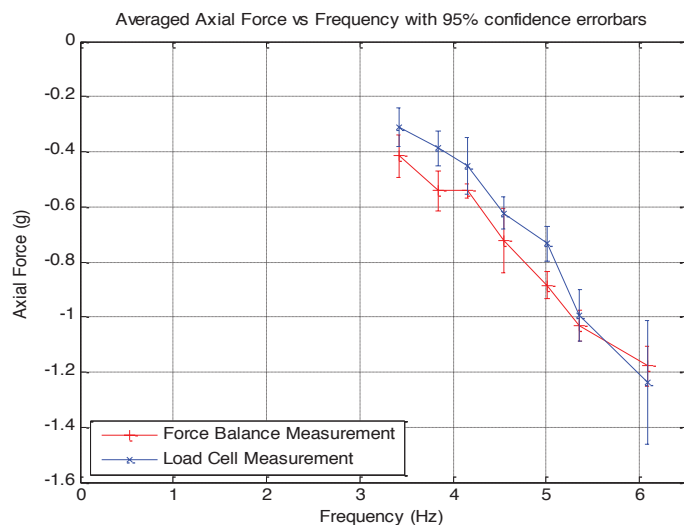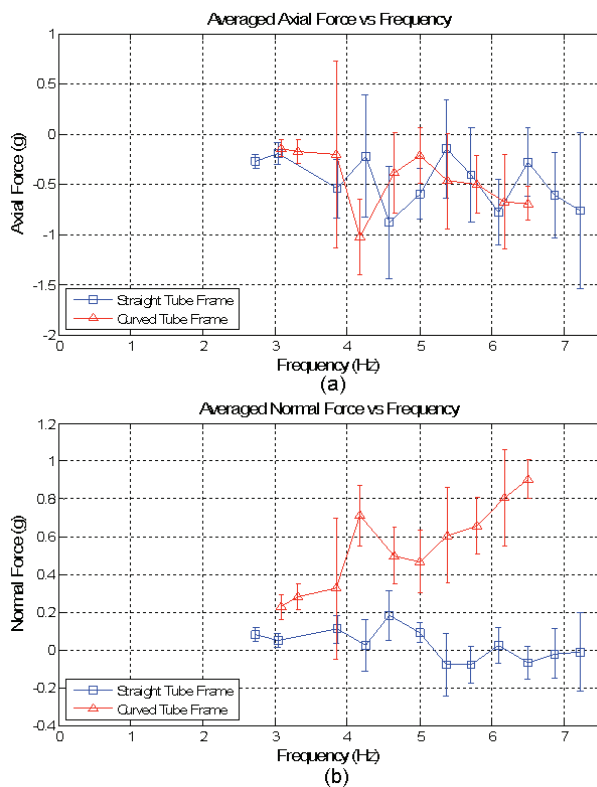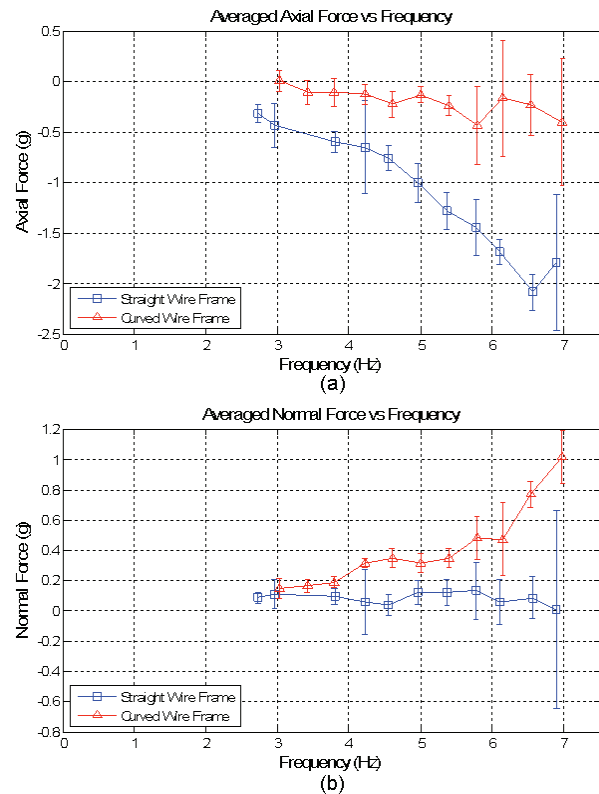

Figure 17. Comparison of load cell to Force Balance measurement technique results. Straight wire frame wings used for testing.

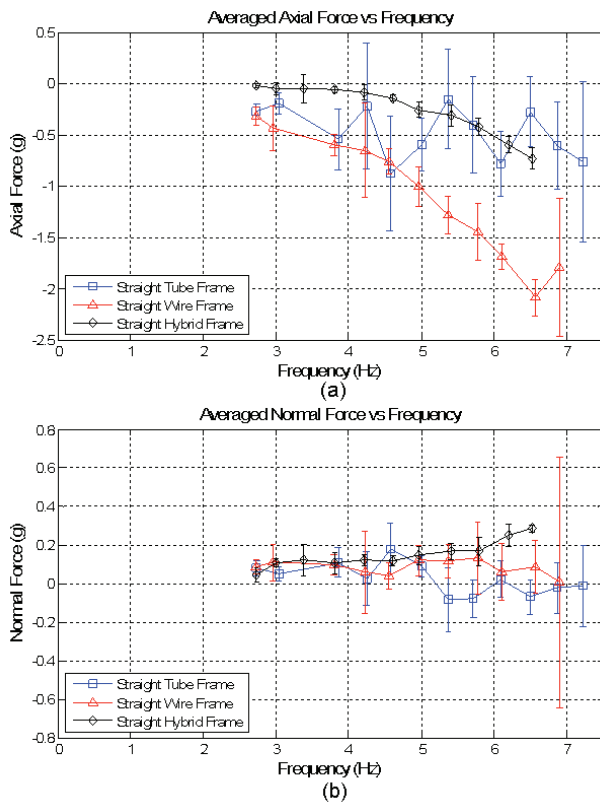**Figure 18.** Comparison of (a) axial and (b) normal force for straight and curved stiff tube frame wings.

Figure 19. Comparison of (a) axial and (b) normal force for straight and curved flexible wire frame wings.

The data presented in Figures 18, 19, and 20 are the averaged values from each run. Since the exact same frequencies were not used for each run, the data points were broken into subsets based on flapping frequency. The frequencies and the force values were averaged within the subset. The length of the error bars was determined based on the number of data points, the standard deviation, and a 95% confidence probability. Since the frequencies are averaged, the calculated standard deviation will be larger than the actual standard deviation supported by the data.

From Figures 18 and 19 it can be seen that applying spanwise camber to the wing does lead to the production of a significant normal force but not axial force. This can be seen in both Figures 18(b) and 19(b) where the curved frame for both cases provides a positive normal force while the straight wings of the same length and width lead to essentially zero normal force. This is consistent with the findings of Hong and Altman [9], who found that for a wing with spanwise camber, the magnitude of the positive force produced on the downstroke is larger than the negative normal force produced on the upstroke. The data in Figures 18(a) and 19(a) suggest that the spanwise camber does not apparently lead to axial force production for this particular case. For the wire frame flexible wings, the straight wings produced more axial force than the curved wing, while for the aluminum framed wing no significant axial force was produced by either wing. This data may be interpreted as meaning that the passive flexure of the wing is important for the production of thrust.

Comparison of the straight wire frame wing to the straight tube frame wing, as in Figure 20, shows a difference only in the axial force. An increasing axial force trend is exhibited only for the wings with flexibility, that is the hybrid frame wings and the wire frame wings, with the most thrust being produced by the most flexible wing set. Ho, Nassef, Pornsinsirirak, Tai, and Ho, observed that flexible wings in flapping produced thrust, while stiff wings did not [17]. Since the attachment point of the wings is at the leading edge, the flexibility will cause the trailing edge to lag behind the leading edge, as demonstrated by Heathcote, Martin, and Gursul [10] and as is evident from Figure 22, at least for a significant portion of the upstroke and downstroke. This lag essentially causes a positive pitch angle on the upstroke and a negative pitch angle on the downstroke, or essentially a positive AoA with regard to the flapping direction throughout the stroke. This allows axial force to be produced in the forward direction throughout the stroke.

Figure 20. Comparison of (a) axial and (b) normal force for straight tube frame, wire Frame, and hybrid frame wings.
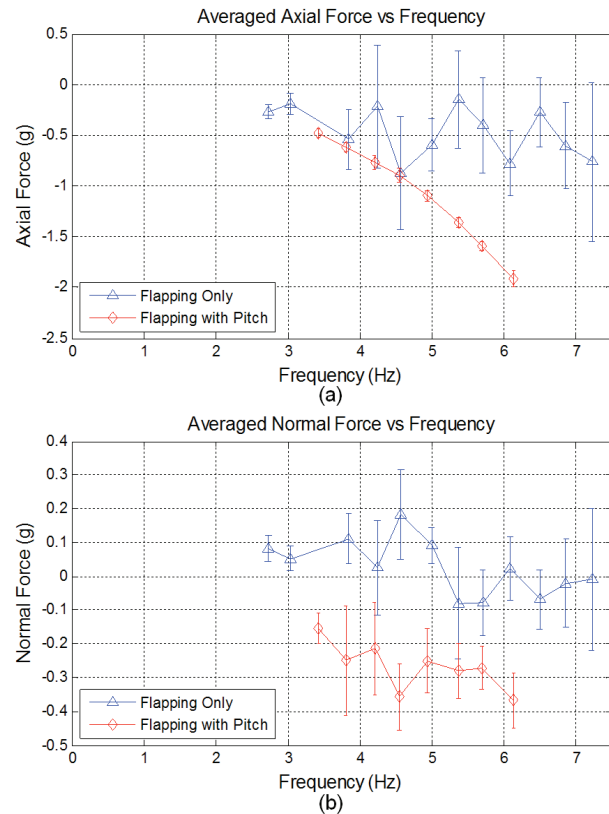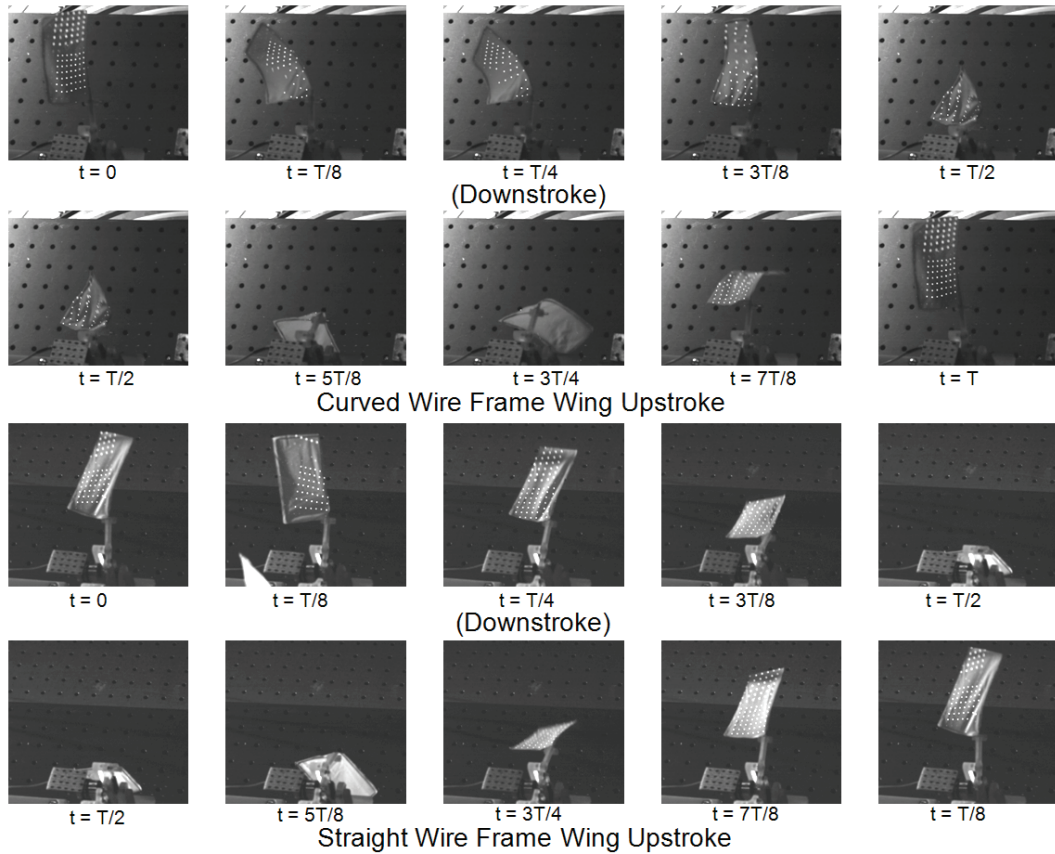

Figure 21. Comparison of (a) axial and (b) normal force for straight stiff tube frame wings for different flapping mechanisms.

Most testing was done with the one degree-of-freedom flapping mechanism, but some force data were taken from the two degree-of-freedom flapping with pitch mechanism. The stiff tube frame straight wings were used with the two degree-of-freedom mechanism. The results are compared to the results from the one degree-of-freedom mechanism using the same wings; they are shown in Figure 21. Notice that by pitching the wing to provide for a positive angle of attack throughout the stroke, axial force is produced. These results are generally in correspondence with the finding of many other researchers [2,3,5,15,18].

C. Photogrammetry and High Speed Imagery

The differences in the normal force between the straight and curved wire frame wings were investigated using images of the wings taken with the high speed cameras. Figure 22 shows the curved and straight wire frame wings at nine locations throughout the stroke for a flapping frequency of approximately 6.2 Hz. Labels show the position in the stroke, where T is the flapping period and is equal to approximately 0.16 seconds. As can be seen, significant flexure of the wings occurs during the stroke. The curved wing appears to be straightening on the downstroke and curving on the upstroke. This could be the reason for this increased lifting force when compared to the straight wing. Also notice that, due to the highly flexible nature of the wing, there are many images in which there is sparse coverage from the laser grid. For this reason, the flexible wings were not selected for initial analysis using the laser dot projection technique.

The stiff tube frame wing sets were chosen for analysis using the laser dot projection method. As can be seen from Figure 23, there is no visible flexure of these wings throughout the stroke. This provides a simpler platform for initial testing of the laser dot projection technique. Because of the time consuming nature of the Photomodeler process, analysis was only done for approximately 25 frames in the upstroke and 25 frames in the downstroke for both the straight and curved wing sets. Images throughout the stroke and from all four cameras are shown in Figure 23.

t = 0	t = T/8	t = T/4 (Downstroke)	t = 3T/8	t = T/2
t = T/2	t = 5T/8	t = 3T/4	t = 7T/8	t = T

Curved Wire Frame Wing Upstroke

t = 0	t = T/8	t = T/4 (Downstroke)	t = 3T/8	t = T/2
t = T/2	t = 5T/8	t = 3T/4	t = 7T/8	t = T/8

Straight Wire Frame Wing Upstroke

Figure 22. Curved (top two rows) and straight (lower two rows) wire frame wing motion at 6.2Hz flapping frequency. Images captured at 1000 fps. Flapping period, T, is approximately 0.16 sec.
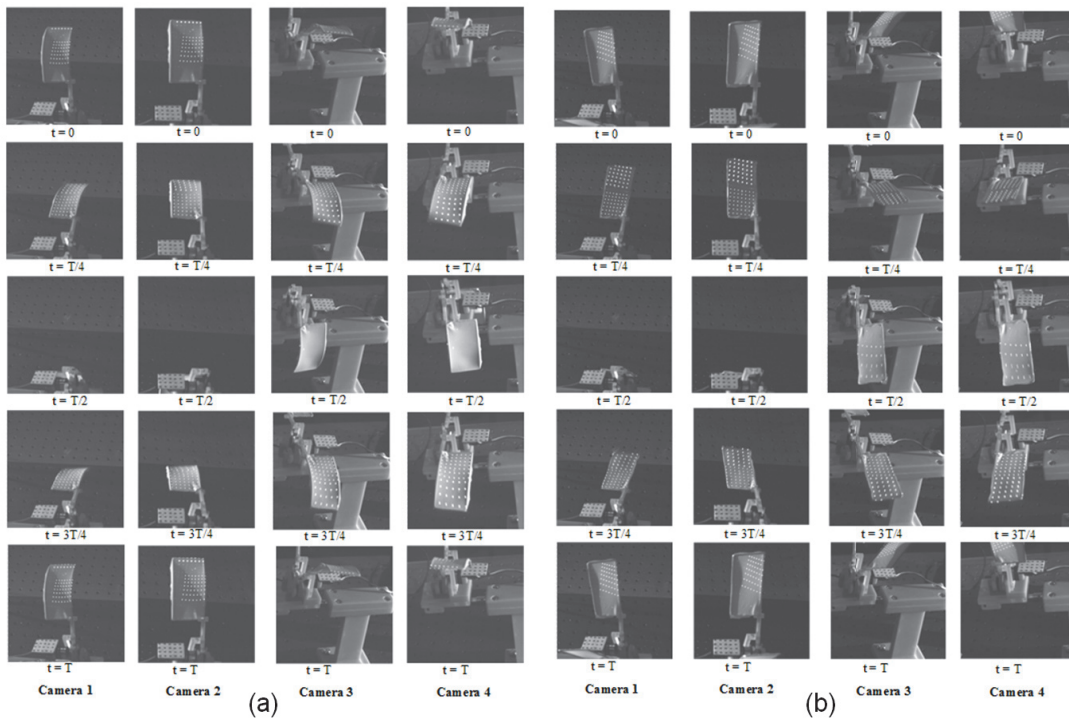

Figure 23. Four high speed camera images of curved (a) and straight (b) tube frame wings with laser dot projection at 6.2 Hz flapping frequency.
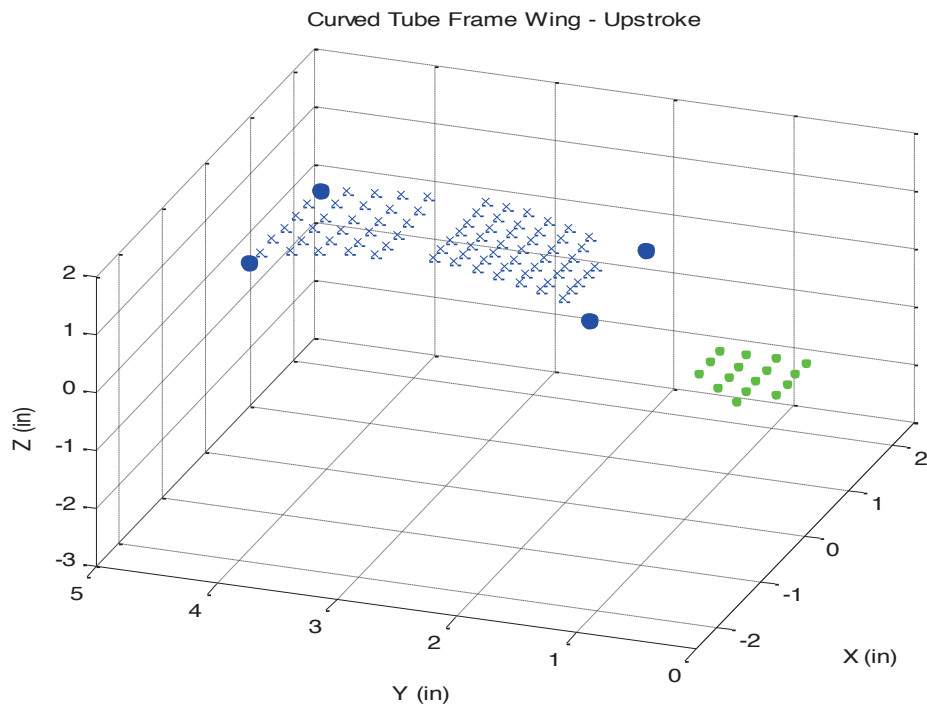
Figure 24. Example plot of 3D point Locations. Solid blue dots represent the physical corners of the wing. Blue 'x' represent laser projection targets. Green dots represent the stationary reference frame. Note that the wing tip is furthest in the positive y-direction and the leading edge is furthest in the positive x direction.

Figure 24 shows the 3D location of each of the laser dots projected on the wing for one set of images; the 3D points at three different locations within each analysis group are shown in Figure 25. The corner points are shown as solid circles. The group of points to the right in the plots represents the grid of stationary reference points used to give scaling and axis direction. The 3D results demonstrate the ability of the laser dot projection method to accurately characterize the kinematic motion of a stiff wing.

For validation of the laser dot projection method of targeting, comparison to traditionally marked targets was required. Marker dots were placed on the wing so that there would be approximately the same number and same spacing as the laser grid. Two of the images used for comparison are shown in Figure 26, and the results from photogrammetry using the two different image sets are shown in Figure27. As can be seen from Figure 27, the marker dots and laser dots are not located at exactly the same position on the wing. Because they aren't located at the same place on the wing, comparing the photogrammetry results using the two methods was not trivial.
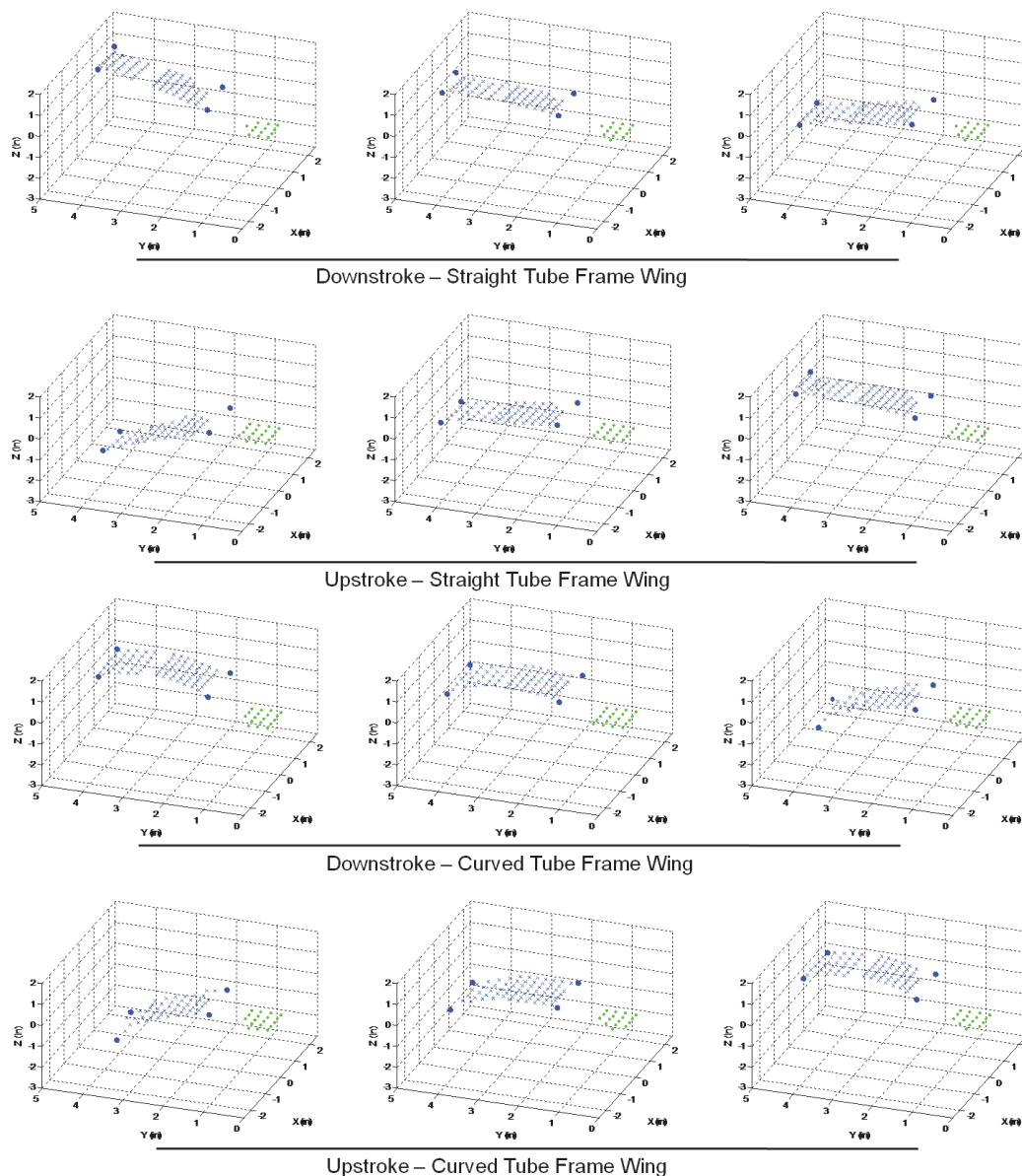
Figure 25. 3D point locations for laser projected dots at 3 epochs in each analysis set. Solid blue dots represent the physical corners of the wing. Blue 'x' represent laser projection targets. Green dots represent the reference frame. Note that the wing tip is furthest in the positive y-direction and the leading edge is furthest in the positive x direction.
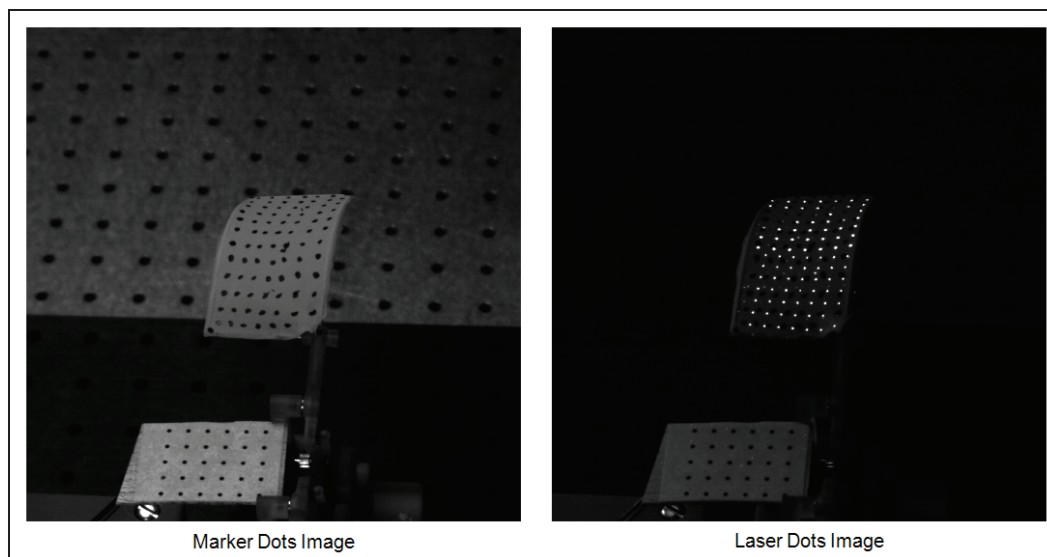
Figure 26. Images Used for Comparison of Marker Targeting to Laser Dot-Projection Targeting. Curved aluminum Frame Wing used.
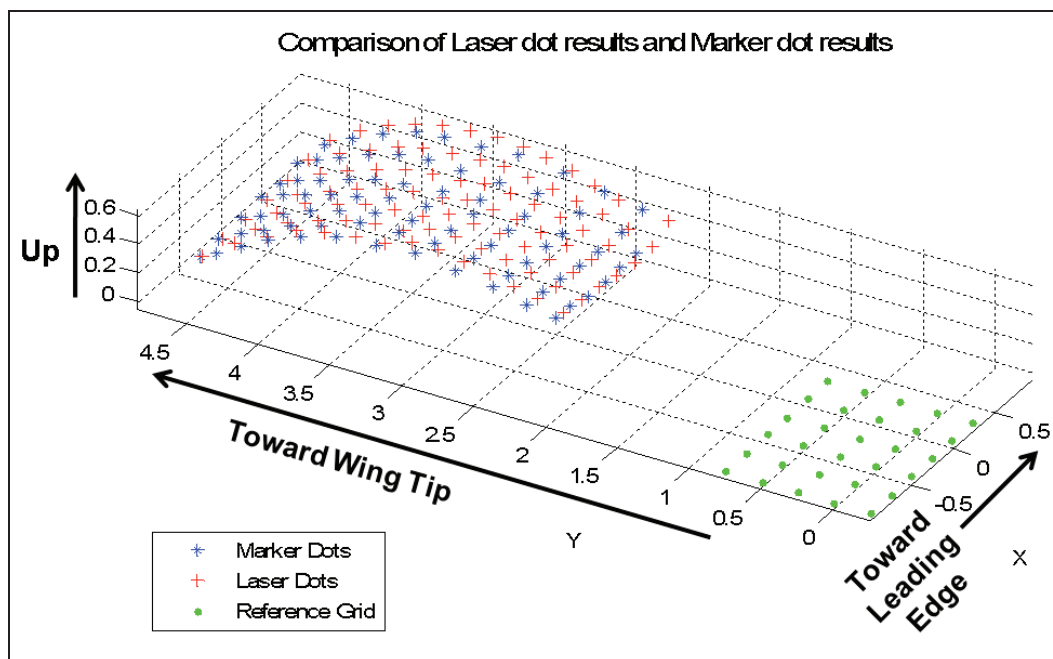
Figure 27. Results from Photogrammetry on Still Wing Using the Two Different Targeting Methods.

In order to compare the results, the shape of the wing surface was mapped using a radial basis function for each case. MatLab codes, available from the MathWorks website, were used to apply this radial basis function method. [19]

The radial basis function method accounts for distance among the network of points. The procedure for calculating a radial basis function is given in reference 20. The radial distance between two points is taken as the square root of the sum of the squares of the difference in each independent variable. In this case the x and y values of the points are treated as the independent variables. The below equation from *Numerical Recipes* is the basis for the radial basis function method.

$$z_j = \sum_{i=1}^{N_k} w_i \phi\left(r_{j,i}\right) \qquad (4)$$

In Equation 4, z_j is an element in a vector of the dependent values, in this case the z-value of the known points; N_k is the number of known data points gathered from the photogrammetry process; $\phi(r)$ is the radial basis function described later; and w is a vector of N_k length which represents the weight of each of the radial basis function values. The radial basis function is a function of the radial distance, $r_{j,i}$, between the jth known or unknown point, and the ith known point. The radial distance is found from the difference in the x-value of the two points, $\Delta x_{j,i}$, and the difference in the y-value of the two points, $\Delta y_{j,i}$, as shown in Equation 5.

$$r_{j,i} = \sqrt{\Delta y_{j,i}^2 + \Delta x_{j,i}^2} \qquad (5)$$

$$\Delta x_{j,i} = x_j - x_i \qquad (6)$$

$$\Delta y_{j,i} = y_j - y_i \qquad (7)$$

In Equations 5-7, x and y constitute arrays of the x-values of the known points and the y-values of the known points respectively, with each having N_k elements. The radial distance, r, of each point from each other point, is determined from the magnitude of the vector between the two points in the x-y plane, as shown in Equations 5-7. These radial distances are inputs to the radial basis function from Equation 4. Essentially this method assumes that the z-value of each known grid point is based on a linear combination of the weighted radial basis function, $\phi(r)$, evaluated at each value of r.

With the assumed value for z_j, this leaves the values within the array represented by w, the weights, as the only unknowns. Evaluating Equation 4 for a single known grid point results in one equation with N_k unknown values in the vector w. By evaluating this equation for each of the N_k known grid points the system of equations is expanded to N_k equations for N_k unknown which can be solved Then, Equations 4-7 can be used to determine the z-value at any value of x and y within the region covered by the known grid.

There are many different types of radial basis functions, $\phi(r)$. Here, the thin-plate spline radial basis function, given by Equation 8, was found to give satisfactory results.

$$\phi\left(r\right) = r^2 \log\left(\frac{r}{r_0}\right) \qquad (8)$$

with $\phi\left(0\right) = 0$

The variable r_0 represents a scale factor which here was set equal to unity. [20] The steps followed to utilize this method are given in references 20 and 21. The radial basis function method described above was done for the results from, alternatively, the marker dots and from the laser-projected dots. A de facto calibration was performed by sampling at known x- and y- positions, and comparing the z-position data. An evenly spaced grid of 20 x 40 points representing a 1" x 2" section in the center of the wing was used for comparison. For each of the grid points, the locations in the z axis for the laser dot surface and for the marker dot surface were determined using the radial basis function method. The average of the absolute value of the difference between the z values of each of the grid points was 0.0109" with a standard deviation of 0.0079". This represents an average difference of approximately 0.4% of the wing's span. Figure 28 shows the surfaces created using the two different sets of data, evaluated over the evenly spaced grid. Notice that for approximately half of the wing, the marker dot surface is higher, while for the other half, the laser surface is higher. In fact, when the difference in the z values of the grid are averaged without taking the absolute values, the result is -0.00022 inches. These results show very close correlation between the two methods, validating the laser dot projection method as an accurate method of non-intrusively determining the overall shape of a surface.
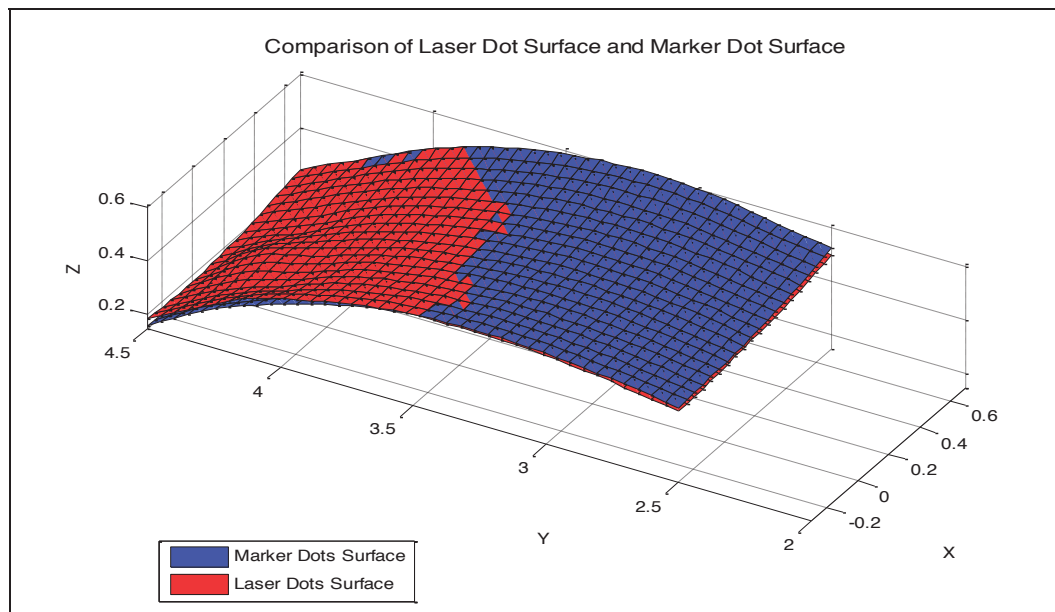
Figure 28. Surfaces Modeled Using the Radial Basis Function through Photogrammetry results from two Different Targeting Methods.

Successful analysis led to the desire to look at wings with more aeroelasticity. For this purpose, the hybrid straight wing was developed and analyzed at the same flapping frequency of 6.2Hz. Images of the wing during flapping, shown in Figure 29, demonstrate that there is noticeable flexure, particularly at the trailing edge of the tip, as would be anticipated from the geometry of the wing.
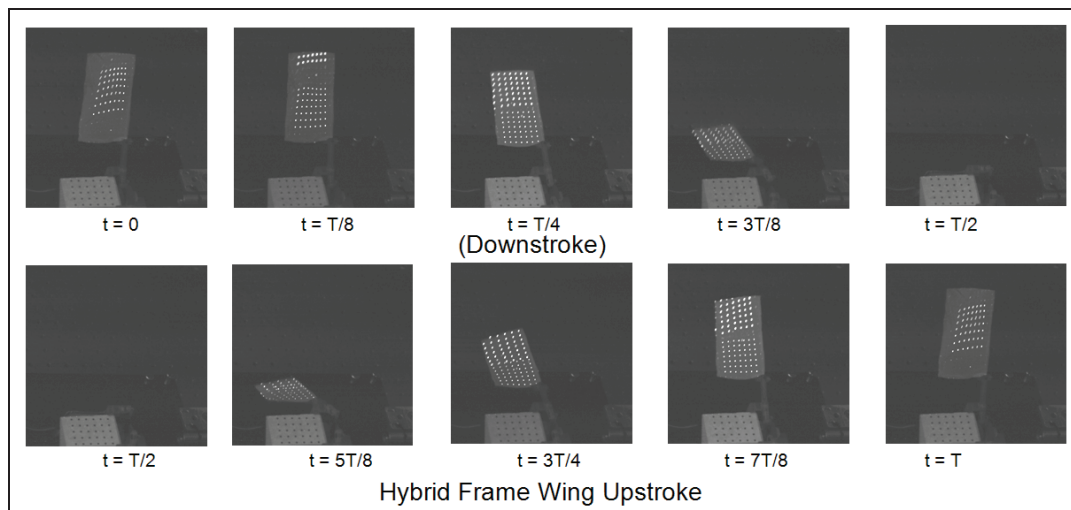
**Figure 29.** High Speed Images of Hybrid Frame Wing Flapping at 6.2 Hz.

Analysis was done on the wing for 30 frames on the upstroke and 30 frames on the downstroke. A surface was modeled through the wing using the radial basis function method described above. The rectangular grid used to create the plots of the surface in Figure 30 contains 20 x 40 regularly spaced points on the wing. The boundaries of the grid in the x direction were found by adding 0.10 inches to the minimum x-value on the laser grid and subtracting 0.10 inches from the maximum x-value on the laser grid. The boundaries in the y direction were found by adding 0.2 inches to the minimum y value on the laser grid and subtracting 0.20 inches from the maximum y-value on the laser grid.

Downstroke – Hybrid Frame Wing

Upstroke – Hybrid Frame Wing
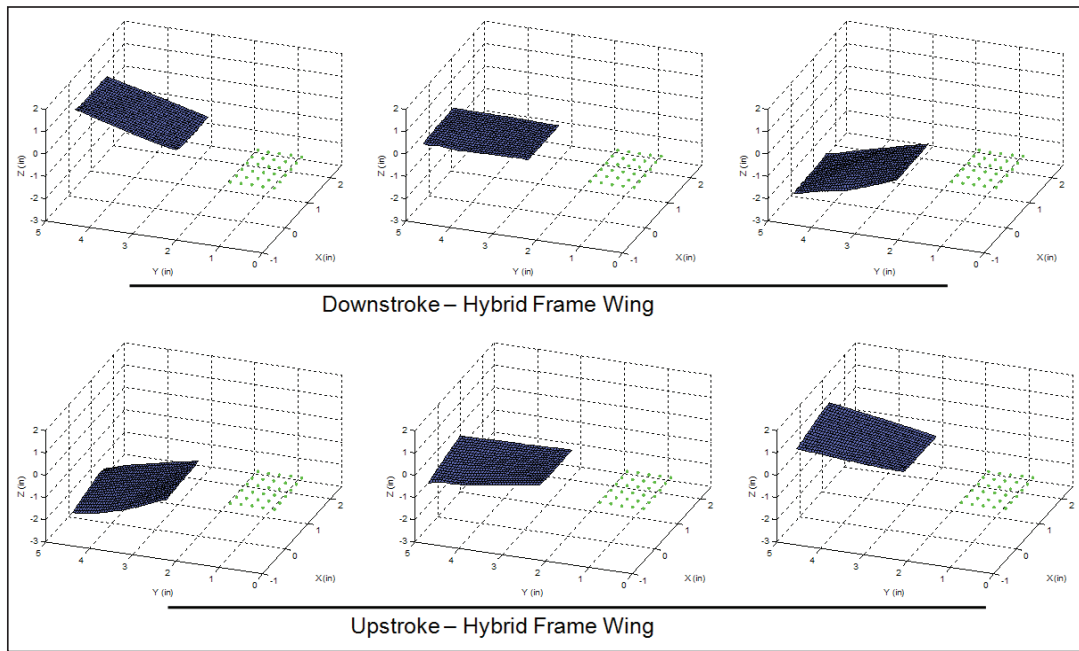
Figure 30. Surface Modeled to Hybrid Wing Photogrammetry results. Blue represents the wing surface, and green dots represent the reference frame.

Approximations of the pitch angle of the root and the tip of the wing were determined from the surface model. The values of the points on the outermost edge of the rectangular grid were used to determine the tip pitch angle. The points were projected into the x-z plane, ignoring the y component, and the slope of a best fit line was calculated. The arc-tangent of the slope of the best fit line was taken as the tip pitch angle. The root pitch angle was determined in the same way with the innermost edge of the rectangular grid. This is an approximate method which diminishes in accuracy as the angle of the wing with the horizontal increases.

In Figure 31(a) a portion of the upstroke and the downstroke, each consisting of the middle of a cycle, are shown. It is evident that in this portion of the cycle, the pitching angle at the tip is significantly higher during the upstroke than during the downstroke. As suggested by other research [10,17], this flexibility could be what is causing the axial and normal forces shown in Figure 20. The fact that the pitching angle at the root is relatively constant through the stroke, as shown in Figure 31(b), is what would be expected from reviewing the frame design in Figure 5.


(a)

(b)
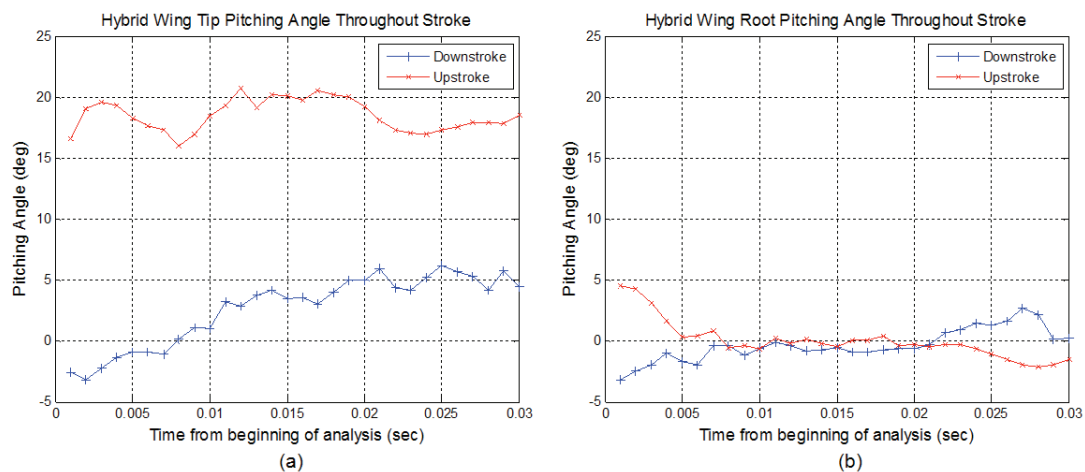
Figure 31. Hybrid wing twist on upstroke and downstroke: (a) Twist at wing tip (b) Twist at wing root.

The way the shape of the wing changes, or the deflection of wing, throughout the stroke can be difficult to visualize because of the flapping motion of the wing. Stewart and Albertani developed an analysis approach that separates rigid-body-motion of the wing from the deformation of the wing during flapping. They used a system to measure the motion of a flat plate, attached to the inboard section of the wing, during flapping. The motion of the flap plate was used to develop a Homogeneous Transformation Matrix (HTM), which was applied to the motion of the flexible portions of the wing. Applying the HTM to the motion of the flexible portion of the wing yields the wing deformation without the wing motion [6].

A simplified approach to that of Stewart and Albertani was taken to quantify the deformation of the wing here. A surface was modeled for the wing at each point using the radial basis function method. A linear best fit line, in the y-z plane, was calculated for the points at the forward most edge of the surface grid. Since the leading edge of this particular wing was made of aluminum, there was minimal flexibility in the spanwise direction at the leading edge, therefore the slope of best fit line is a good approximation of the flapping angle. The approximate location of the pivot point for the wing was estimated by averaging the intersection points of the best fit lines from each frame. The pivot point and the flapping angle were used to adjust the y and z values for each grid point to the wing reference frame. The wing reference frame origin is located at the pivot point, and reference frame moves with the wing according to the flapping angle. Finally a surface was modeled to the adjusted grid system. Essentially this method yields an estimate of the flapping angle by simulating the wing as a rigid flat plate. The surface in the new reference frame is essentially the difference between the surface formed by a flapping rigid flat plate and the surface from the actual wing during flapping. Results are shown for one frame during the downstroke and one frame during the upstroke in Figure 32 and Figure 33 respectively. These figures clearly show the difference in the pitch of the wing tip between the upstroke and the downstroke, as is demonstrated in Figure 31. This process isolates the wing deformation by subtracting the flapping angle.
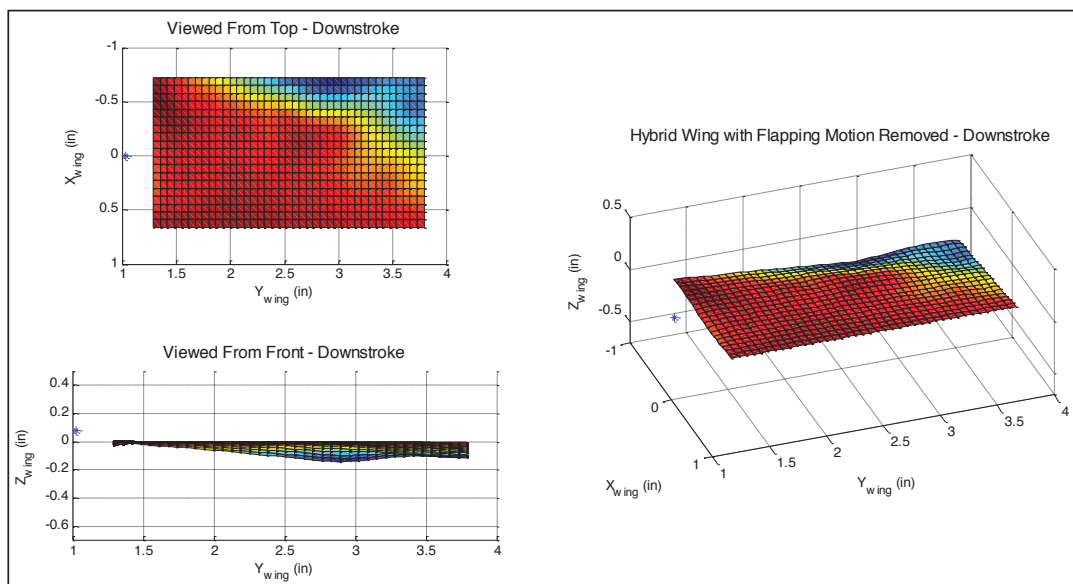
Figure 32. Deformation of the Hybrid Wing in the Wing Reference Frame for one frame in the downstroke.
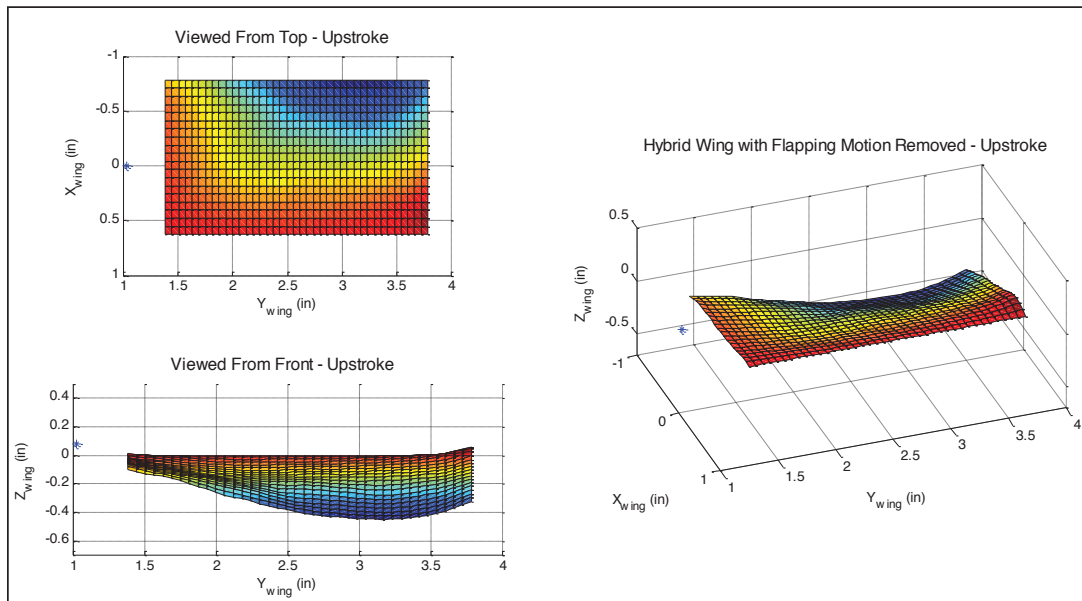
Figure 33. Deformation of the Hybrid Wing in the Wing Reference Frame for one frame in the Upstroke

6. CONCLUSION

Through a cooperative effort between AFIT and the Air Vehicles Directorate of the Air Force Research Laboratory, a static bench test setup was developed in order to gain a better understanding of Micro Air Vehicles, specifically those with flapping wings. It is critical to have the tools to assess the performance of micro air vehicles in order to establish whether and how a specific design might outperform others. To this end, a variety of different tools have been developed to assess flapping-wing MAV performance, and the main focus of this paper is to outline these measurement approaches. Leading into this work, it was necessary to build and test flapping-wing mechanisms.

Flapping-wing mechanisms were designed and built with many parts derived from solid modeling tools and built with a 3-D printer. Initially, an air bearing table was used in combination with a load cell to collect time-averaged thrust data for a one-dimensional flapping mechanism with wings designed to passively vary pitch. The measured motor power draw was measured along with the thrust measurement to determine power and thrust coefficients, which led to a figure of merit. This approach was found to be useful for broadly characterizing the designs, despite the limitation to a single force component and time-averaged measurements.

The bench test setup was substantially improved through the use of a 6-component balance and photogrammetry. Data from the balance, low-pass filtered at 200 Hz, were acquired, and average axial force measurements acquired from the balance were generally comparable to that acquired using the air bearing table. A significant portion of our work was dedicated to experimenting with the photogrammetry system to measure wing location and deformation in conjunction with a dot-projection technique. A portion of the upstroke and of the downstroke of a flapping wing operated at a specific frequency was analyzed using images acquired from the four-camera system. Proof-of-concept data were acquired for a wing having a relatively stiff frame and with curvature applied along the span. The results, specific to that wing shape, show the ability to track the kinematic motion of the stiff wing during flapping.

Significantly, the photogrammetry data capture system successfully employed laser dot projection, in lieu of physical markings on the wings in order to reduce, if not eliminate, intrusiveness. A validation of the laser dot projection method was done on a still wing by marking the curved tube frame wing with marker dots in a grid with approximately the same spacing as the laser grid. A radial basis function interpolation method was used to model the shape of the wing and to compare results from photogrammetry using the two targeting methods. The average difference between the two shapes from the two different target types provided assurance that the laser dot projection approach is appropriate. A hybrid wing was developed in order to demonstrate the ability of the laser dot projection in studying

flexibility. A shape was modeled to the wing, and the pitch of the wing throughout the stroke was investigated. The wing was found to demonstrate flexibility that both is in-line what would be expected from the wing design as well as justifies the force measurements that were taken. A simple method of subtracting the flapping motion of the wing from the photogrammetry results in order to view only the shape change of the wing was developed. The dot projection technique, which utilized structured light from small diode lasers, proved to be a useful way to collect wing location and deformation data for flapping wings suitable for micro air vehicles.

REFERENCES
[1]   Banala, Sai K. and Agrawal, Sunil K., "Design and Optimization of a Mechanism for Out-of-Plane Insect Winglike Motion with Twist," *Journal of Mechanical Design*, Vol. 127, July 2005, pp. 841-844.

[2]   Issac, K.M., Colozza, Antony, and Rolwes, Jessica, "Force Measurement on a Flapping and Pitching Wing at Low Reynolds Numbers," *44th AIAA Aerospace Sciences Meeting and Exhibit*, AIAA Paper 2006-450, AIAA, Reno, Nevada, Jan. 9-12, 2006.

[3]   Wilson, Nicholas L. and Werely, Norman, "Experimental Investigation of Flapping Wing Performance in Hover," *48th AIAA/ASME/ASCE/AHS/ASC Structures, Structural Dynamics, and Materials Conference*, AIAA Paper 2007-1761, AIAA, Honolulu, Hawaii, Apr. 23-26, 2007.

[4]   Singh, Beerinder, and Chopra, Inderjit, "Insect-Based Hover-Capable Flapping Wings for Micro Air Vehicles: Experiments and Analysis," *AIAA Journal*, Vol. 46, No. 9, 2008, pp. 2115-2135.

[5]   Jadhav, Gautam, and Massey, Kevin, "The Development of a Minature Flexible Flapping Wing Mechanism for Use in a Robotic Air Vehicle," *45th AIAA Aerospace Sciences Meeting and Exhibit*, AIAA Paper 2007-668, AIAA, Reno, Nevada, Jan. 8-11, 2007.

[6]   Stewart, Kelly, and Albertani, Roberto, "Experimental Elastic Deformation Characterization of a Flapping-Wing MAV Using Visual Image Correlation," *Critical Technology Development for Micro Munition Vehicles, TTCP Meeting*, Aberdeen Proving Ground, Maryland, 16-17 October 2007.

[7]   Pappa, Richard S., et al, "Dot-Projection Photogrammetry and Videogrammetry of Gossamer Space Structures," *Journal of Spacecraft and Rockets*, Vol. 40, No. 6, 2003, pp. 858-867.

[8]   Pennycuick, C.J., "Span-ratio Analysis used to Estimate Effective Lift:Drag Ratio in the Double-Crested Cormorant Phalacrocorax Auritus from Field Observations," *J. Exp. Biol.* Vol. 142, pp 1-15, 1989

[9]   Hong, YoungSun, and Altman, Aaron, "An Expiremental Study of Lift Force Generation Resulting from Spanwise Flow in Flapping Wings," *44th AIAA Aerospace Sciences Meeting and Exhibit*, AIAA Paper 2006-448, AIAA, Reno, Nevada, Jan. 9-12, 2006.

[10] Heathcote, S., Martin, D., and Gursul, I., "Flexible Flapping Airfoil Propulsion at Zero Freestream Velocity," *AIAA Journal*, Vol. 42, No. 11, 2004, pp. 2196-2204.

[11] Rojratsirikul, P., Wang, Z., and Gursul, I., "Unsteady Aerodynamics of Membrane Airfoils," *46th AIAA Aerospace Sciences Meeting and Exhibit*, AIAA Paper 2008-613, AIAA, Reno, Nevada, Jan. 7-10, 2008.

[12] Liu, Tianshu, Kuykendoll, K., Rhew, R., and Jones, S., "Avian Wing Geometry and Kinematics," *AIAA Journal*, Vol. 44, No. 5, 2006, pp. 954-963.

[13] Curtis, D., Reeder, M., Svanberg, C., and Cobb, R.. "Flapping Wing Micro Air Vehicle Bench Test Set-up," *47th AIAA Aerospace Sciences Meeting Including the New Horizons Forum and Aerospace Exposition*, AIAA Paper 2009-1272, AIAA, Orlando, Florida, Jan. 5-8, 2009.

[14] Svanberg, Craig E., "Biometric Micro Air Vehicle Testing Development and Small Scale Flapping Wing Analysis," Masters Thesis, Aeronautics and Astronautics Dept., Air Force Institute of Technology, WPAFB, OH, 2008.

[15] Dickinson, Michael H., Lehmann, Fritz-Olaf, and Sane, Sanjay P., "Wing Rotation and Aerodynamic Basis of Insect Flight," *Science*, Vol. 284, No. 5422, 18 June 1999, pp. 1954-1960.

[16] Noonan, K., Yeager, W., Singleton, J., Wilbur, M., Mirick, Paul H., "Wind Tunnel Evaluation of a Model Helicopter Main-Rotor Blade with Slotted Airfoils at the Tip," NASA TP-211260, Dec. 2001.

[17] Ho, S., Nassef, H., Pornsinsirirak, N., Tai, Y., Ho, C.M., "Unsteady Aerodynamics and Flow Control For Flapping Wing Flyers," *Progress in Aerospace Sciences*, Vol. 39, 2003, pp. 635-681.

[18] Birch, J. and Dickinson, M., "The influence of wing-wake interaction on the production of aerodynamic forces in flapping flight," *J. of Exp. Biol*. Vol. 206, pp 2257-2272, March 2003.

[19] Wiens, Travis. "Thin Plate Spline Network with Radiohead Example," MatLab script available at <www.mathworks.com>. 22 July 2008 [cited 15 Jan. 2009]

[20] Press, W. H., Teukolsky, S. A., Vetterling, W. T., and Flannery, B. P., *Numerical Recipes, The Art of Scientific Computing*, 3rd ed., Cambridge University Press, Cambridge, UK, 2007.

[21] Curtis, David H., "Laser Dot Projection Photogrammetry and Force Measurement for Flapping Wing Micro Air Vehicles," Master's Thesis, Aeronautics and Astronautics Dept., Air Force Institute of Technology, WPAFB, OH, 2009.